4 Detector Design

The detector upgrade proposed for CLEO II is divided into charged particle tracking and charged particle identification. The particle identification technology is undetermined at this time although the minimum criterion is 4σ π/K for particles with momentum up to 2.8 GeV/c. The charged particle tracking system must perform a number of functions which include measurement of the charged particle momentum and angles, locating the vertex for charm and tau decays, particle identification using $\mathrm{d}E/\mathrm{d}x$, and providing information for the trigger. The tracking system must meet the following criteria under high luminosity conditions :

- It must operate with short bunch spacing, large beam currents, increased background rates, and with quadrupoles within its boundaries.
- It must allow 20 cm for particle identification.
- It must provide track resolutions, mass resolutions, and vertex resolutions which are comparable to or better than those achieved with CLEO II.

The global features of the design are based on the analytical calculations of track resolutions and full Monte Carlo simulations of pattern recognition with background noise, track finding, and track reconstruction for the physics processes discussed in the simulation section. The details of the design draw heavily on the experience of the CLEO collaboration.

A side view of the CLEO III detector is duplicated in Fig. 29. Tracking detectors fill the radial region from just outside the beampipe at r=2.2 cm to r=82 cm. The space between 82 cm and 102 cm is reserved for particle identification. The angular coverage is defined by the IR quadrupoles which restrict the available solid angle to 93% of 4π. The silicon detector consists of four layers at radii of 2.5, 3.75, 7.5, and 10.0 cm; a low mass drift chamber begins at a radius of 17.5 cm and extends to 82 cm with approximately 43 sense wire layers. The magnetic field is 1.5 Tesla.

The distinctive feature of this design is in the separation of the tracking functions between the silicon and the drift chamber. The drift chamber dominates the measurement of momentum, and the silicon dominates the measurement of $\cot\theta$ and z vertex. Both devices share equally in the measurement of ϕ and the impact parameter. This separation of functions is a natural consequence of extending the radial length of the silicon and reducing the length of the drift chamber to accommodate the IR quadrupoles and particle identification. To compensate for this restriction and ensure no compromise in momentum resolution, the drift chamber inner wall is made of beryllium and its gas must have a radiation length of 332 m, twice that used in CLEO II (50% Ar, 50% C_2H_6).

In the following section the details of the various devices are described. The options and R&D plans for the various detector sub-systems are also discussed.

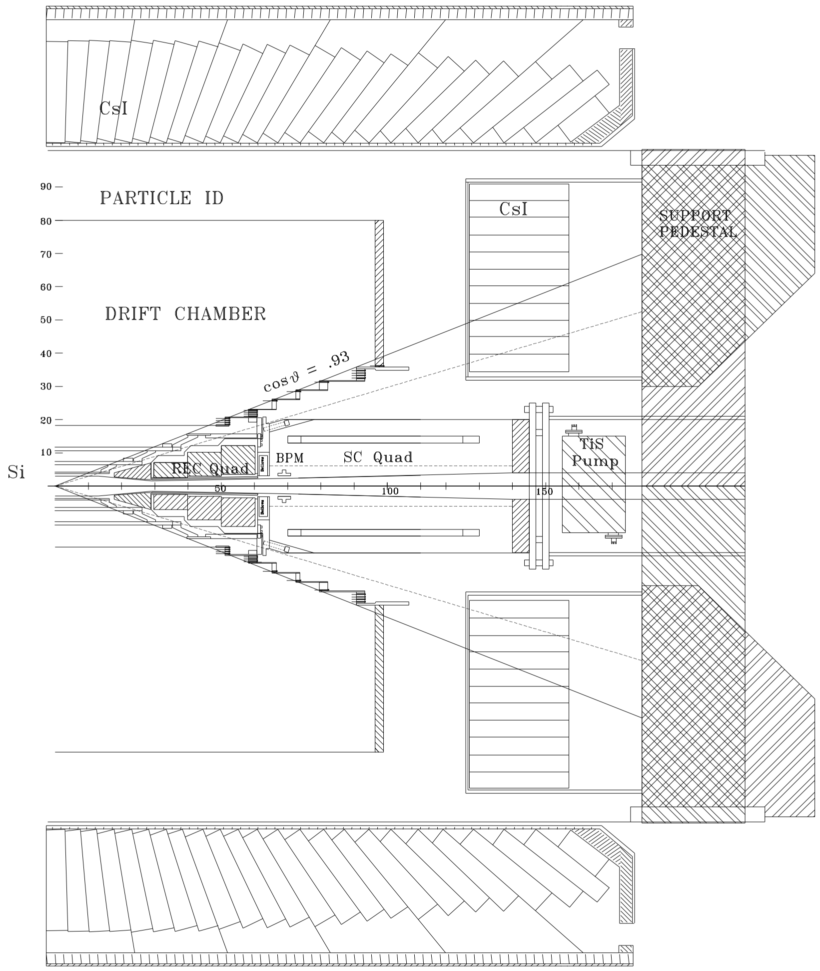

Figure 29: A half-section view of the CLEO III detector inside the superconducting solenoid and the CESR Phase 3 interaction region components. The 20 cm clear space around the drift chamber is reserved for the particle identification system—the detector technology is yet to be determined.

4.1 Beampipe

The beampipe for the present CLEO upgrade (to be installeded in September 1994) is designed for the same beam intensity as for the CLEO III upgrade. It consists of a 2 cm radius, double-wall beryllium cylinder with 0.5 mm gap for water coolant, and can maintain a 3°C water temperature rise for 400 W of heat deposit over its 30 cm length.

The total material amounts to 0.6 % of radiation length, half from 10 μm of gold coating which absorbs synchrotron radiation and the rest approximately equally shared by water and beryllium. The mechanical structure has been analyzed by a finite element program and the buckling pressure was found to be 14 atm of outside pressure for an infinitely long tube. Since the actual structure has both ends fixed to circles, this estimate is a conservative one, and was confirmed by a three dimensional numerical model. Extensive corrosion/erosion and flow tests have been performed with positive results.

For the CLEO III upgrade, the radius of the beampipe will change to 2.2 cm. This will make the structure slightly weaker but still well within the buckling point. Experience from the CLEO II silicon detector operation will determine if it is possible to reduce the gold thickness below 10 μm.

4.2 Silicon

4.2.1 General detector parameters

In this section we describe the silicon vertex detector. The exact parameters given will probably change as the design evolves and we try to optimize the overall design, but at the present time the design provides a working model of sufficient detail to permit us to estimate some performance characteristics.

The silicon tracker consists of four layers of double sided silicon strip detectors starting at r = 2.5 cm, ending at r = 10.00 cm, and filling 93% of the solid angle. The design summarized in Table 15 can be assembled from $\sim$ 500 identical detector modules, each 2.4 cm $\times$ 6.5 cm $\times$ 300 μm. In this baseline model we assume the p- and n-side strips are orthogonal, though other stereo angles may be considered. We assume the beampipe outer radius is 2.2 cm with 3 mm clearance to the first layer. The other detectors are placed at radii that are integral multiples of a common base value (1.25 cm in this case) in order to maintain simple scaling relationships among all the layers. With this approach we generate a design in which the full detector can be built entirely from identical devices, thereby reducing costs and simplifying the testing and R&D. This simplicity will also propagate outward to the external electronics and the mechanical structure.

Figures 30 and 31 show the $r\phi$ and rz views of the proposed detector. In the $r\phi$ view one sees that the detectors overlap each other by approximately 2 mm in order to facilitate

Table 15: Arrangement of layers and detectors

Layer	Radius (cm)	# Detectors in ϕ	# Detectors in z
1	2.50	8	2
2	3.75	12	3
3	7.50	24	6
4	10.00	32	8

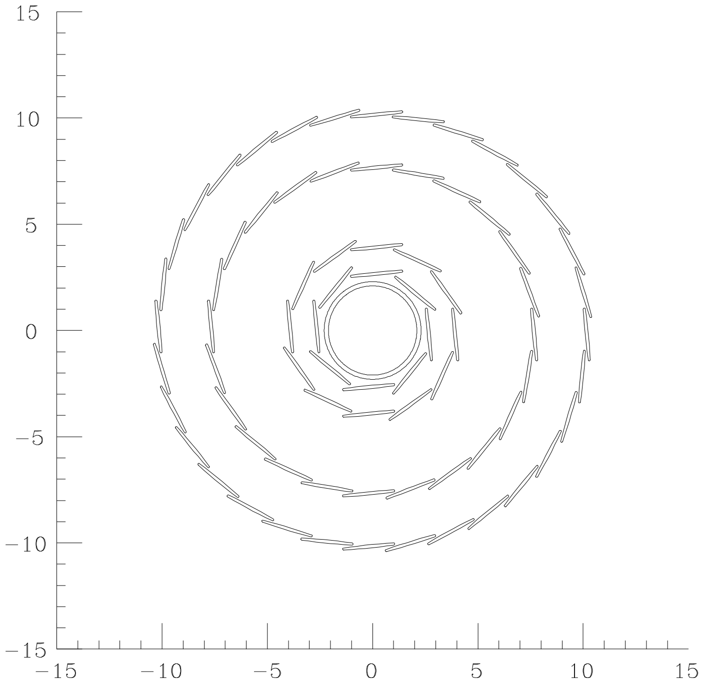

Figure 30: Transverse section through proposed silicon detector.

alignment; the rz view illustrates the lengthwise daisy chaining of detectors. The left and right ends of the detector are read out separately and the detectors are not joined in the middle. In layer 2, where an odd number of detectors (3) span the length, one readout handles one detector, and the other readout handles two detectors.

Readout of the z-side information is an important issue. This design is based on the double layer design used in the CLEO II silicon vertex detector, in which z strips, perpendicular to the ϕ strips, are read out via longitudinal traces on top of an insulating layer of SiO_2. The CLEO II detector design is illustrated in Fig. 32. Our final design will differ from the CLEO II design in many important respects, but some form of the double layer readout structure will have to be incorporated into the CLEO III detectors, so the CLEO II design provides a convenient starting point. For the time being we assume the z-side is the n-side, as in CLEO II, but plan to examine this choice more carefully at a later date.

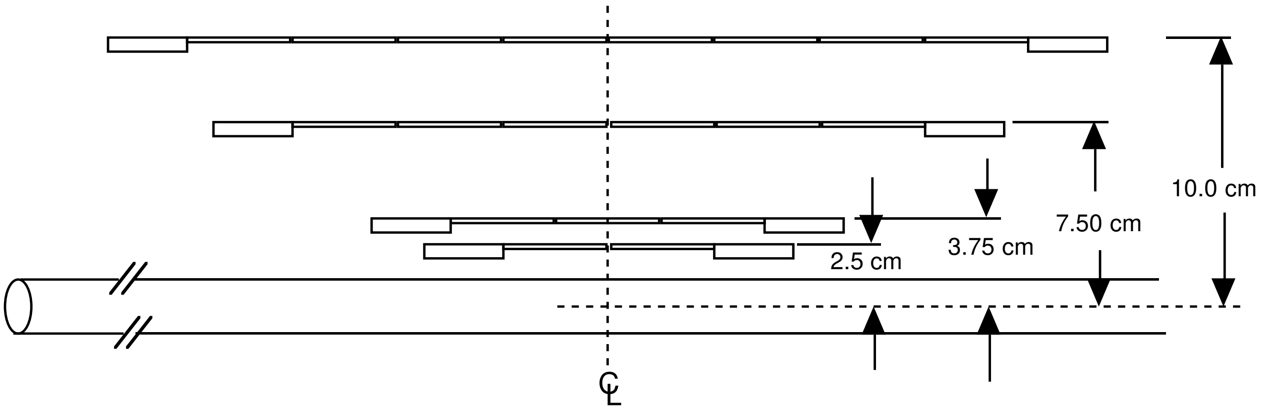

Figure 31: Longitudinal section through proposed silicon detector. The length scale is compressed a factor of two relative to the radius scale.

Figure 33 shows the layout of traces and strips on the two sides of the detector. Note that all longitudinal traces and strips have a pitch of 44 μm, and on the n-side, the sense strips have a pitch of 124 μm. These choices are the result of the following considerations:

1. With the detector dimensions fixed by simple geometric considerations given above, the $r\phi$ pitch is then chosen such that the number of readout channels is 512, to be compatible with using, for instance, four 128-channel readout chips.

2. Strips on the z-side must be mapped 1:1 onto readout traces, without ganging strips into one readout channel. Ganging leads to increased noise and in some ways complicates pattern recognition. The daisy chaining of multiple detectors already imposes an unavoidable ganging which must not be increased. The rather large pitch on the z-side, 124 μm is a result of this restriction. In order to keep all detectors identical, the pitch is constant.

3. No floating strips may be used on the z-side. While it is common practice to employ floating strips in a detector to reduce the strip pitch without increasing the number of readout channels, it is not possible to use such strips on the z-side. Capacitance to the overhead, orthogonal readout traces would trap some fraction of the signal charge, dispersing it across all channels and thereby effectively losing it. At a later point in this document we will discuss some options for reducing this capacitance, but it is unlikely to be small enough to overcome this restriction. On the $r\phi$-side we also dispense with floating strips because with the small (44 μm) pitch they are not necessary.

4. Granularity is not an issue. Estimated backgrounds yield layer 1 occupancies of 0.05% per strip for the expected beam currents, the proposed shielding, a 1 μs integration time in the preamplifiers, and the above choice of pitch. This is negligible and, therefore, plays no role in determining strip pitch.

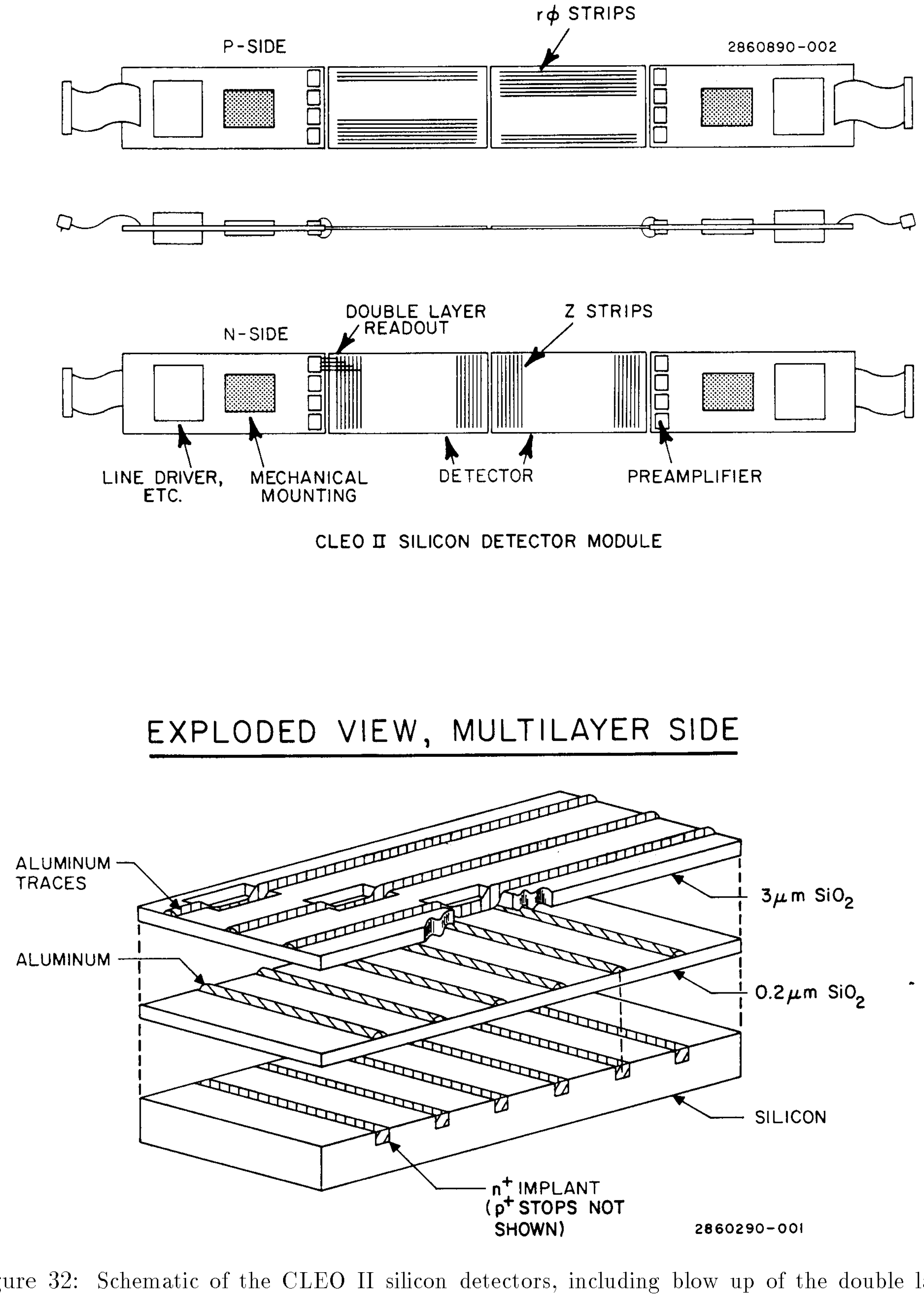

Figure 32: Schematic of the CLEO II silicon detectors, including blow up of the double layer structure showing sense strips and longitudinal readout traces with contact vias.

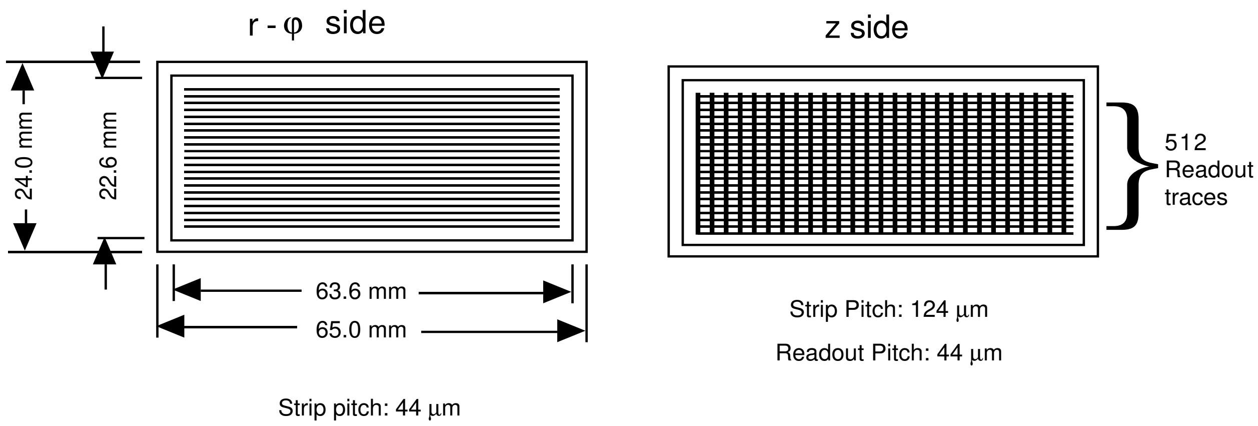

Figure 33: Schematic of proposed detector strip layout.

We note that 44 μm is not a convenient match to existing readout chips, and are exploring alternative designs that permit use of a standard 50 μm input pitch.

4.2.2 Resolution

Resolution is intimately connected with choice of pitch, the signal to noise ratio (S/N), and the algorithm used for clustering pulse heights. It depends, in addition, on the angle of the incident track as this determines both the number of strips crossed by the track and the mean pulse height on each strip. We have simulated energy deposition and carrier transport and diffusion in a silicon detector in a stand-alone Monte Carlo. Cluster position is the pulse height weighted mean of the first and last strips in a cluster, with a minimum cut on pulse height required. Figure 34 shows the resulting resolution for the z and $r\phi$ sides of the detector, respectively, as a function of the angle of incidence of the track, for three values of S/N = 10, 15, and 20. We see that for the higher values of S/N the resolution is dominated mainly by the choice of strip pitch and by Landau fluctuations with a less strong dependence on S/N. For lower values of S/N, however, the resolution of steeply inclined tracks degrades rapidly. For S/N=15, we average over angles and find in z, $\sigma \sim 24\mu m$, and in $r\phi$, $\sigma \sim 10\mu m$.

In light of these results, we take our target for detector and electronics design to be $S/N \geq 15$ when all sources of noise and degradations of signal are taken fully into account.

4.2.3 Capacitance

Detector capacitance plays a key role in determining S/N. By "detector capacitance" we refer to the sum of all parallel capacitances that load the preamplifier front-end. These may be categorized as follows:

1. Interstrip capacitance (C_{is}) between sense strips. It can be usefully parametrized[77, 78]

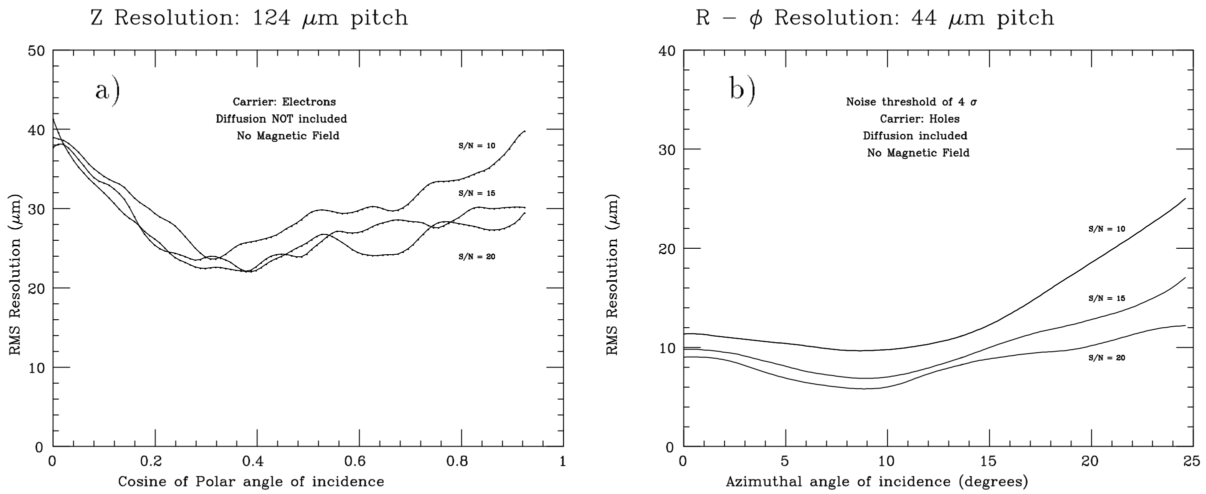

Figure 34: a) The calculated z resolution as a function of incidence angle for various S/N ratios. b) The calculated $r-\phi$ resolution as a function of incidence angle for various S/N ratios.

by

$$C_{\text{is}} = (0.87 + 1.61\frac{w}{d})L \tag{14}$$

where w is the strip width, d the pitch, and L the length in cm. All capacitances discussed here are in pF.

2. Backplane capacitance (C_{back}) between a sense strip and the opposite side of the detector. We note that

$$C_{\text{back}} = \epsilon\frac{Ld}{t}$$

where $\epsilon = 11.9\epsilon_0$ is the dielectric constant of silicon, $\epsilon_0 = 8.85$ pF/m, L and d are the strip length and pitch in centimeters, and t is the detector thickness in millimeters.

3. Interreadout capacitance (C_{ir}) between longitudinal readout traces on the z-side. This cannot be calculated with Eq. 14 as for interstrip capacitance because some of the field lines terminate on the sense strip electrodes, and thus contribute to the overlap capacitance (see below). In general, it is less than the interstrip capacitance.

4. Overlap capacitance (C_{ov}) between the longitudinal readout traces on the z-side and the electrodes of the z strips themselves. Each overlap contributes a capacitance of order $\sim$10 fF, but the exact value depends on the widths of the traces, the pitch of the z strips (and for n-type z strips, the width of the gap between the p isolation strips), and the thickness and dielectric constant of the material insulating the readout traces from the sense electrodes. For n:1 ganging of strips, and N readout channels, it is easy to show that the total overlap capacitance loading one channel is given by $2n(N-1)C_{\text{ov}}$ which can easily be of order 10 pF.

5. Stray capacitance ($C_{\rm stray}$) is the presence of miscellaneous capacitances due to structures not accounted for in the above list, and we allow typically 1–3 pF for this contingency.

We have estimated the capacitance of the proposed detector units, and in Table 16, compare the proposed detector with the CLEO II (layer 1) detectors. For the CLEO II detectors we have measured both the individual contributions to the total capacitance, and the total capacitance of a single strip. We find the sum of the "exclusive measurements" matches the "inclusive measurement" almost perfectly on the p-side, and there is a 10% shortfall on the n-side. That shortfall is within errors, but it may also represent some small components not taken into account (such as direct capacitance between strip and readout traces).

The key differences are the absence of ganging in the new detector, and a modest reduction in the overlap capacitance, $C_{\rm ov}$, which we will achieve by narrowing the n-side effective strip width from 36 μm to 18 μm and increasing the SiO_2 thickness from 3 μm to 5 μm. Since edge effects play a dominant role in this capacitor, we do not anticipate a large impact from these changes, but assume we can reduce $C_{\rm ov}$ by about 25%. Note that the effective strip width for the n-strips is not just the width of the strips, but that plus the region of accumulation layer, out to the p-isolation strip. This directly affects the size of the overlap capacitance. Use of kapton readout circuits, glued directly to the detector, could avoid the need to build the double layer readout, and may slightly reduce the associated capacitances, but appears to be practical only in cases where the aspect ratio of the detector is modest. In our case, where we have an aspect ratio of about 10:1 in the outer layer, such readout may not be so useful. Nevertheless, we intend to follow closely the experience of other groups using or planning to use this technique.

To be safe, we inflate the estimated z-side capacitance per detector to account for any possible missing capacitance. Thus for the z-side, we estimate $C_d = (\frac{27.5}{24.6}) \times 16.7$ pF $= 18.7$ pF. Taking the most difficult case, layer 4, we see that the preamplifiers will have to deal with a load of approximately 36 pF on the p-side and 75 pF on the n-side.

4.2.4 Readout

In Table 17 we summarize performance figures of existing and planned VLSI preamps. Some of the noise figures listed here are estimates or are based on prototypes only.

Based on noise performance alone, two chips look attractive and can be considered candidates at this point. The JAMEX and the VIKING both achieve noise figures of about 150 + $15C_d$ in equivalent noise charge (ENC). Taking these numbers at face value, we conclude that for the layer 4 z-side, the total noise would be $\sim 150 + 15{\times}75 = 1275$ electrons. Absent any other sources of noise, barring shortfall in performance, and ignoring issues of availability and reliability, these chips would just permit S/N$\sim$13.5 (see section on signal size below).

Table 16: Capacitances in the CLEO II and Proposed Detectors.

p-side	CLEO II	Proposed Detector
Strip Length (cm)	6.0	6.5
Strip Pitch (μm)	112	44
Strip Width (μm)	10	8
C_{is} (pF)	6.1	7.5
C_{back} (pF)	2.4	1.0
C_{stray} (pF)	0.5	0.5
Sum of Individual Capacitances (pF)	9.0	9.0
Observed Total Capacitance (pF)	9.1	–

n-side		
Strip Length (cm)	2.12	2.26
Strip Pitch (μm)	105	124
Strip Width (μm)	20+16	8+10
Ganging	3:1	1:1
C_{is} (pF)	$3 \times 2.7 = 8.1$	2.5
C_{back} (pF)	$3 \times 0.75 = 2.3$	1.0
C_{ov} (pF)	$6 \times 188 \times 8fF = 9.0$	$2 \times 511 \times 6fF = 6.2$
C_{ir} (pF)	3.2	4.0
C_{stray} (pF)	2.0	3.0
Sum of Individual Capacitances (pF)	24.6	16.7
Observed Total Capacitance (pF)	27.5	–

Table 17: Summary of available and planned readout chips.

	Chip	Expt.	# ch	Pitch μm	ENC	$\tau_{\rm RAD}$ (kRAD)	$\tau_{\rm int}$ μs	Power mW/ch
•	CAMEX64	ALPH/CLII	64	100	$340+31C_d$	25	$\sim$1	$\sim$2.0
	CAMEX128	(none)	128	50		never made		
•	JAMEX	CLEO II	64	100	$150+15C_d$	$\sim$ 100's	$\sim$1	$\sim$6
	AMPLEX	UA2	16	200	$300+35C_d$	NA	0.8	1.1
•	VIKING	DELPHI	128	50	$135+12C_d$	50+	2.0	$\sim$1
•	MX3	DELPHI	128	50	$350\sqrt{C_d+3.5}$	15	?	.5–1
	MX5	OPAL	128	55	$325+23C_d$	5	?	1.3
	MX7		128			hard		
	KEK-proto	KEK	128	50	1400 @20pF	NA	$\sim$1	NA
	KEK-Bfac	KEK	128	50	1000 @20pF	NA	$\sim$1	NA
•	SVX Rev H3	CDF, L3	128	50	$300+33C_d$	1000	$\sim$1	1.8
	SVX-II	D0	128	50	$330+57C_d$	1000	0.132 adj	3.0
	ARC	(FNAL)	128?	50?	$600+50C_d$	NA	0.132 adj	1.3

NA = information not available

•= CLEO collaborators have experience with these chips

We can expect further noise sources (see section on noise, below), which will degrade this S/N ratio. Moreover, the JAMEX pitch would force 2:1 ganging which will increase the capacitance and the noise; our experience so far with the JFET-CMOS process on which the JAMEX is based is that it is unreliable and yields are low.

Nevertheless, we find it encouraging that existing chips may already meet at least the noise performance requirements. In a later section we will discuss in more detail some explicit detector designs which are less demanding on the electronics than the baseline detector.

Other considerations besides noise will also figure into any decision about preamplifiers. The backend of the preamplifier should match the data acquisition system requirements—the chips listed above differ in the features they offer. To meet the DAQ requirements, it is desirable for the silicon front-end IC to incorporate analog to digital conversion, sparsification, and data buffering, such as are available in the SVX-II. It is not necessary that multiple events be buffered if the conversion time plus the time for data transfer to the off-detector electronics is 10–50 μs.

Since there are several hundred hybrids, depending on design, it is imperative that the number of signals routed to and from them be minimized. To reduce the bulk of the cable plant it is desirable that the data be transferred off-detector serially. Likewise, a single clock should control the data recording sequence and other control information, such as event trigger and configuration should be done serially. To further reduce the cable plant, the serial links should be provided at the hybrid level, not at the IC level. Power distribution should also be at the hybrid level and the number of voltages sent from the outside to the hybrids needs to be limited. Two voltages and a return are ideal—one voltage for the preamp/storage/back-end and one for depletion.

Although backgrounds and, hence, radiation damage are generally expected to be low in CLEO III (see backgrounds section), rad-hard CMOS processes are readily available and provide cheap insurance against the unexpected and the catastrophic. As can be seen from Table 17, such processes provide for hardness at the megarad level. We assume that all on-detector electronics will be rad-hard.

4.2.5 Signal

A minimum ionizing particle traversing 300 μm of silicon deposits charge that is approximately Landau distributed with the peak of the distribution occurring at 78 keV[79]. This corresponds to 21,500 electron-hole pairs generated.

In AC coupled detectors there are non-negligible losses due to finite charge collection efficiency. Signal charge deposited on a strip is shared among all capacitances directly coupled to that strip, including capacitance to the nearest neighboring strips, to more distant neighbors, to the opposite side of the detector, to overhead readout traces, and, most importantly, to the readout electrode. Denoting the last capacitance as C_c, the coupling capacitance, we see that the signal collection efficiency is given by

$$\epsilon_{\text{signal}} = \frac{C_c}{C_c + \sum_{i=1}^{n} C_i}$$

where the C_i are all the capacitances listed above. Any capacitance on the preamplifier side of the coupling capacitor does not enter the sum, unless it happens also to contact the sense strip, as in the case of capacitance to overhead readout traces. For the CLEO II detector, where we have measured most of these capacitances, we estimate a signal collection efficiency from the above formula to be between 80 and 85%, allowing for uncertainties in the measurements. In practice we observe an efficiency around 80%, or a signal size of about 17,000 electrons.

Clearly any realistic estimation of S/N in an AC coupled design must take into account collection efficiency. While maximizing C_c will drive $\epsilon \to 1$ in the above formula, technical constraints will limit how far this game can be safely and cost-effectively played.

AC coupling is generally desirable because it provides some immunity from detector dark currents and permits stable pedestals. The integration of the coupling capacitors into the detectors, however, as in the CLEO II detectors, may not be the best choice for the future as it lowers the detector yield, raises the costs, and hampers detector testing. External coupling capacitor chips look promising, and good designs[80] include clamping diodes to protect against catastrophic damage.

DC coupling should not be ruled out. Nearly full signal recovery can be achieved with the large dynamical capacitance typical of charge integrating amplifiers, and that will help in achieving maximal S/N. In addition, the relative simplicity of a DC coupled system (no integrated capacitors, no external capacitor chips) makes it attractive—and probably cheaper than an AC coupled system.

4.2.6 Noise

Noise originates from both the detector and the preamplifier. The detector noise is dominated by three terms:

1. Shot noise. Statistical fluctuations in the arrival of charge carriers in the detector leakage current lead to a noise term contribution

$$ENC^2 = 2qI_{\text{leak}}|\mathcal{F}|^2\tau$$

   where τ is the peaking time of the amplifier and $\mathcal{F}$ is the transfer function to propagate the noise from the source point to the front of the amplifier. This source is typically small, contributing 100–200 electrons of noise, but each detector in a daisy chain adds a new and independent source, so the total noise from leakage current scales as $n^{1/2}$ where n is the number of detectors strung together.

2. Bias resistor noise. Thermal noise in the bias and feedback resistors constitutes a parallel noise source leading to a contribution

$$ENC^2 = \frac{4kT}{R_B}|\mathcal{F}|^2\tau.$$

In the CLEO II detectors this is significant only on the n-side where, with three $20M\Omega$ bias resistors in parallel, the net contribution is about 200 electrons. Again, this source also scales with $n^{1/2}$.

3. Trace resistance noise. Finite resistance, R_r, in aluminum readout traces gives rise to a series noise source with

$$ENC^2 = 4kTC_d^2R_r|\mathcal{F}|^2$$

for the (relevant) case in which C_dR_r is small compared to the integration time of the amplifier[81]. The detector capacitance appears in the equation because it provides the path through which the noise current loop is closed. In the CLEO II detectors, this source is negligible on the p-side but may be significant on the n-side where the combination $C_d\sqrt{R_r}$ is about 4 times larger. In any case, we note that this contribution scales as $L^{3/2}$, where L is the length of the detector array. For detectors of a given length, this means the noise will scale as $n^{3/2}$ which is a stronger dependence than for the other two terms and needs to be watched.

An important aspect of detector design thus consists of ensuring that the detector noise sources remain small compared to the amplifier noise. The basic ideas are clear from the simple scaling laws illustrated above: keep R_B large, R_r small, and, as always, minimize the detector capacitance. For daisy chained groups of detectors it is important to take into account the scaling with $n^{1/2}$ and $n^{3/2}$ as noted above. For the purposes of analyzing the detector proposed here, we will assume that we can achieve a detector noise comparable to the 250 electrons we presently observe on the p-side of the CLEO II detectors, and will scale with n as appropriate. We note, however, that the n-side of the CLEO II detectors exhibits more noise than is accounted for by the three sources listed above, and we are still working to understand this additional component. Such n-side effects have also been noted by others[82].

In reality we must deal with a slightly more complex case, namely, with detectors that are multi-strip objects. On the z-side in particular, the cross-coupling between strips is not entirely negligible and multi-strip effects must be taken into account. We have found it useful in the development of the CLEO II detector to model the detector in some detail to understand how noise from various sources propagates through the complicated RC network that describes the multi-strip detector. The detector model is based on a set of detector measurements[83] and standard network analysis techniques, and it reproduces the measured transfer functions of the detectors.

The final noise figures from all sources i, $(i = 1...n)$ are calculated by summing incoherently over sources and integrating over frequency-dependent transfer functions:

$$ENC^2 = \frac{1}{\pi}\int_0^\infty |\mathcal{F}_{\rm C}(\omega)|^2 \sum_{i=1}^{n} \left(\frac{dI^2_{\rm RMS}}{d\omega}\right)_i |\mathcal{F}_i(\omega)|^2 d\omega.$$

In this formula, $\mathcal{F}_{\rm C}(\omega)$ is the transfer function of the amplifier, $\mathcal{F}_i(\omega)$ is the transfer function from the i^{th} source to the front of the amplifier, and $(dI^2_{\rm RMS}/d\omega)_i$ is the spectral power density for the i^{th} source. This kind of modelling will be used in designing the new detectors to minimize the detector noise contribution.

In general, amplifier noise dominates. It arises from two main sources:

1. White noise. Fluctuations in the bias current of the front-end transistor give rise to a thermal noise current in the channel just as they do in a resistor, and have a spectral noise density given by
$$\frac{dI^2_{\rm RMS}}{d\omega} = \frac{1}{2\pi} 4kT\,\frac{2}{3} g_m,$$
where g_m is the transconductance of the transistor. Referring this channel noise to the gate gives a voltage that is impressed across the sum of detector capacitance and input (gate-source) capacitance of the front transistor, and consequently the noise:
$$ENC^2 = (C_d + C_i)^2 \frac{4kT}{3\pi g_m} \int_0^\infty |\mathcal{F}_C(\omega)|^2 d\omega,$$
or $ENC = A + B \times C_d$. The actual noise figure that one can achieve will depend on the transistor design (through g_m) and the shaping (through $\mathcal{F}_C(\omega)$). Table 17 illustrates that, despite widespread effort, achieving a noise slope below 15/pF is not an easy task.

2. $1/f$ noise. In addition to this thermal noise source, there is also $1/f$ noise which arises from trapping and detrapping of charge carriers in and near the channel. Such effects can dominate the noise characteristics of CMOS devices where the charge transport occurs primarily at the defect-ridden silicon-SiO_2 interface; in JFET's charge transport is deeper in the bulk silicon, and such effects are less important, leading to overall better noise performance. The spectrum (referred to the gate again) is given by:
$$\frac{dV^2_{\rm RMS}}{d\omega} = \frac{2\pi F}{WL}\frac{1}{\omega},$$
where W and L are the transistor width and length, and F is an empirical factor that depends on the process. The JAMEX amplifier differs from the CAMEX in that JFET's are used in place of MOSFET's in the noise-sensitive parts of the amplifier, and this underlies the factor of 2 improvement in the noise performance.

To achieve $S/N \geq 15$ requires that we realize $ENC \leq 1200$ after summing over both detector and amplifier sources, and assuming the signal collection efficiency is comparable to what we achieve in CLEO II. Improving the signal collection by DC coupling or reducing the noise will improve S/N and help provide some margin of safety.

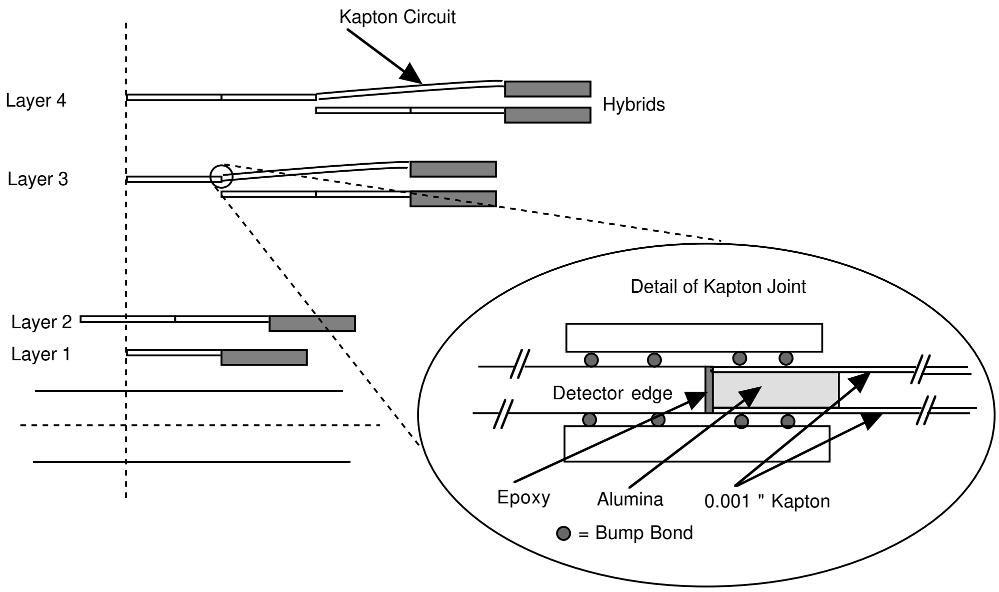

Figure 35: Longitudinal section of proposed detector, showing split layers and kapton readout circuits.

4.2.7 Design options

We now examine two possible designs for the CLEO III silicon detector.

Design one: *Brute Force*

This design follows the CLEO II design closely. Detectors are daisy chained in z in each layer, as necessary, with all preamps located outside the tracking volume. Fig. 31 illustrates this design. With the detector parameters as defined in Table 16 we find total capacitance ranges from 9 pF for the p-side of layer 1 to 75 pF for the n-side of layer 4.

The distinctive feature of this design is that it places all the burden on the preamplifier. In Layer 4, with four detectors daisy chained, we can estimate that the detector noise will be approximately $\sqrt{4}$ times the noise of one detector. Amplifier noise must therefore be less than 1090 electrons, which implies the noise slope must be better than $11e$/pF, assuming an input capacitance of 25 pF. To judge by the noise slopes shown in Table 17, this is ambitious[84]. The burden on the preamplifiers is therefore substantial, and there is little margin for error. The detectors, however, are relatively simple, and this is the main advantage of this design.

Design two: *Modified Brute Force*

In this design we avoid some of the large capacitance of the brute force design by using kapton flex circuits to provide low-capacitance, low-mass readout lines. We require the detectors in layers 3 and 4 to be staggered radially, as shown in Fig. 35. Then, at most two detectors are daisy chained together, and the innermost pairs of detectors are read out by kapton circuits, as shown in the figure. A simple and robust means of attaching the kapton circuits to the detectors is illustrated schematically in the inset.

Table 18: Comparison of the two options

Option	Advantage	Disadvantage
(1) Brute Force	•Simple detectors •Cheaper detectors •Could start detectors today •CLEO II experience is directly applicable	•Difficult electronics? •No fall back position if electronics slips
(2) Modified Brute Force	•Same detector advantages as above •Electronics achievable •Could start today •High confidence of success	•Mechanically more difficult •More electronics channels •Backend electronics needs development

Each 0.001 inch thick kapton circuit has a thickness of 0.008% X_0, and copper traces of 6 μm thickness and 12 μm width[85] will add another 0.01% X_0, for a total of about 0.02% X_0, or about 1/15 of a silicon detector thickness. The interstrip capacitance on the kapton circuits is estimated for a 13 cm length of kapton circuit with strip pitch 44 μm and strip width 12 μm to add about 6 pF. In layer four, therefore, the z-side will see a worst case capacitance of $2 \times 19 + 6 = 44$ pF. This is less than the capacitance in the layer 3 z-side of the CLEO II detector.

This design has the advantage of simple detectors, as in the previous "brute force" design, but the demands on the preamplifier are much reduced. A noise slope of 18/pF would yield a total amplifier noise of approximately 1150 electrons, and with the detector contribution the total would be under 1200. The design is also robust in allowing a fall-back position in which no detectors are daisy chained, but every detector is connected either directly, or through a kapton circuit, to a preamplifier. This increases the number of channels, but reduces the capacitance per channel and eliminates all ganging.

The principal advantage of this design is that it breaks little new ground and could be started today with high confidence of success.

Comparison of the two options

In Table 18 below we compare the advantages and disadvantages of the options proposed above.

4.2.8 R&D

We list below some of the areas where R&D should begin.

- We will study the capacitance of a large variety of 3-dimensional structures, especially crossed strips, with different geometries and dielectric media. Experimental measurements and development of code to permit calculation of capacitance between arbitrary structures in 3D will be done. Such expertise will form part of the technical underpinning of the detector design.
- We will study the properties of kapton circuits in close detail, to understand the capacitance, trace conductivities, and dielectric noise.
- High resistance p-side and n-side biasing will be studied. Polysilicon will not suffice. We will pursue an early design that we tested but did not retain for CLEO II, in which MOSFET's are operated close to pinch-off. For such operation, the variation in the threshold voltage from one transistor to the next, across the detector, could be important and will be studied. Other alternatives include moving the bias resistor and AC coupling capacitor off the detector.
- Radiation damage in detectors, particularly if MOSFET's are used as described above, will be tested. We will use the CHESS facility for such investigations, as we have done previously in assessing the radiation hardness of the CAMEX. Radiation damage in readout electronics will also be evaluated.
- We will investigate available IC bonding technologies to determine their applicability to our assembly. The efficiency of the bonding procedure is important and vendors will be tested with prototype production.
- Noise studies in the CLEO II detectors will be brought to a conclusion. The remaining n-side noise sources will be identified.
- Full scale detector prototypes will be constructed within the first year since our experience with CLEO II was that the full scale detectors with double layer readout exhibited features not present in small test structures. We are presently working with a variety of vendors to come up with designs they can mass produce cost-effectively.
- Engineering evaluation of the front-end readout electronics requirements, especially the noise performance and power dissipation requirements is critical and available chips will be tested.

4.3 Drift chamber

The present CLEO II tracking system, including the Precision Tracking Layer detector (PTL), Vertex Detector (VD), and Drift Chamber (DR 2), has shown that it can perform under high luminosity conditions. The addition of a silicon detector will enhance the system. Therefore, we use the *attained* CLEO II tracking performance as a benchmark for CLEO III. This includes excellent momentum resolution, $dp/p < 0.56\%$ at $p = 1$ GeV/c, excellent angular resolution, $\sigma_{\tan\theta} \sim 0.004$, and good impact parameter resolution, $\sigma_{\rm IP} < 75$ μm (< 35 μm when the silicon is added). These tracking parameters translate directly into the resolutions of physics variables. For example, the D^*-D^0 mass difference resolution is presently $\sim$1 MeV which provides a 40:1 signal to background for D mesons tagged by this method. The present CLEO II tracking system performance has been achieved by using a 1.5 Tesla magnetic field, $\sim$0.8 m long tracking length with minimal material, and good spatial resolution—50 μm in the PTL, 100 μm in the VD, and 150 μm in DR 2. The goal of the CLEO III drift chamber is to attain comparable or better tracking performance while allowing 20 cm of space for a particle identification system and space for the high luminosity interaction region quadrupoles.

4.3.1 Mechanical overview

The momentum resolution of a tracking system depends primarily on the *uninterrupted* tracking length, the amount of scattering material, the number of measurements, and the magnetic field. For good momentum resolution, the drift chamber must fill the available space as completely as possible. It must also allow room for the insertion of the inner detector and for a 20 cm particle identification device at the outer radius. The inner radius is limited to 17.5 cm by the support system of the silicon vertex detector and the assembly procedure for the interaction quadrupoles. This places the first sense wire layer at 18.8 cm. The physical outer radius has been limited to 82 cm, 12 cm less than the current CLEO outer drift chamber[88], providing 20 cm of radial space for particle identification in front of the CsI crystal holder. After allowing space for an outer support skin and segmented cathode readout on the outermost layer, the available active tracking length is $\sim$62 cm with the final sense layer radius at 79 cm. The longitudinal dimension of the detector can be the same as that of the current drift chamber, 94.0 cm inside the endplates, and is limited by the existing CLEO magnet, the endcap calorimeters, and the endcap particle identification systems. Additional space for the particle identification device in the endcap region will be provided by freeing longitudinal space currently used for the interaction quadrupole support. This has the immediate advantage that the obstructions of the barrel crystal calorimeter due to the endplates and, more importantly, the stiffening ring at the outer radius of the endplates, are moved to a larger $|\cos\theta|$.

To maximize the polar angle coverage while providing access to the mounting points for the vertex detector and accommodating the intrusion of the interaction quadrupole, we have chosen a multi-step endplate design as shown in Fig. 36. Such a design allows interleaving of the IR quadrupoles and the drift chamber endplate to obtain maximal detector solid angle. The positions of these steps will depend on the final IR quadrupole design and the exact cell size and shape employed. These issues are presently under study in our R&D program.

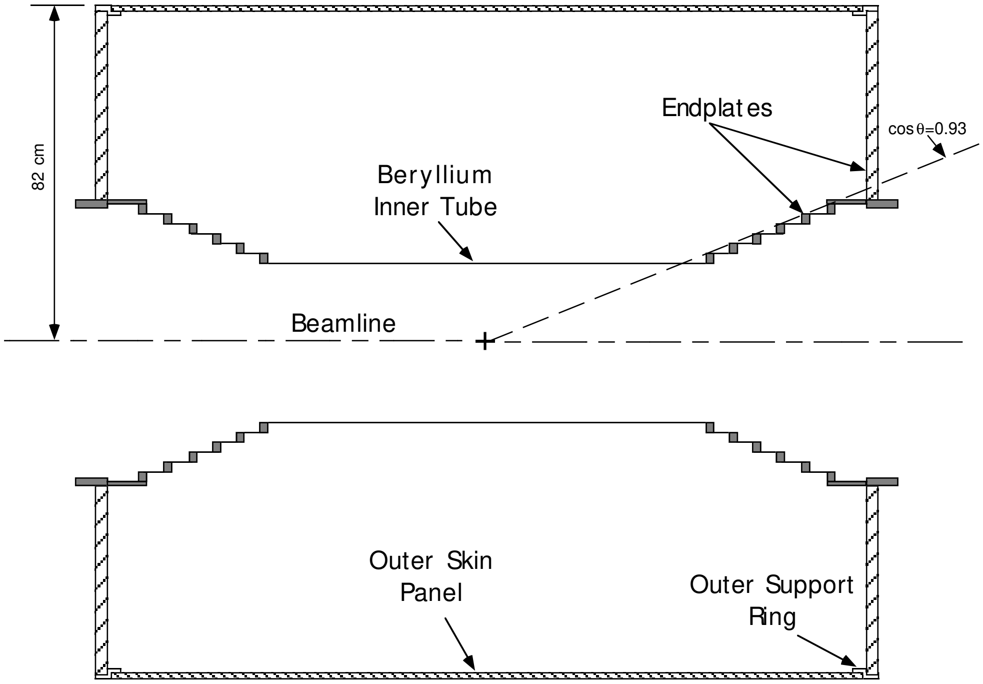

Figure 36: Drift chamber structural design.

Using a similar cell design and wire holding scheme to the present CLEO chamber, the polar angle can be extended to $|\cos\theta| = 0.93$ with 12 layers in the stepped sections followed by a section of flat endplate with 31 layers, providing a total of 43 sense wire layers.

Wire tension will be held at the outer radius by composite skin panels with an aluminum thickness of 1.6 mm as in the current CLEO drift chamber. We have found that these panels (total thickness of 2% X_0) do not degrade the electromagnetic calorimeter in back of them, and we have tested the strength of this system at 10 times the required load. An inner beryllium tube, 0.5 mm thick (0.15% X_0), will be used as an inner gas seal and may hold some of the wire tension. It also provides mechanical protection and RF shielding with the minimum material between the inner detector and the drift chamber measurement volume.

Reducing and redistributing the material in the drift chamber is also important for maintaining or improving the performance of the CsI calorimeter and may have substantial impact on the particle identification system. To date, most CLEO II analyses only use the "good barrel" region of the calorimeter, $|\cos\theta| < 0.7$, for candidate photons because elsewhere the efficiency has been lower and the background higher, due in large part to material in front of the calorimeter. In the proposed detector, the "good barrel" region will extend out to $|\cos\theta| < 0.77$, with the endcaps covering $0.77 < |\cos\theta| < 0.93$. This is the result of the main drift chamber having a smaller radius and a different support scheme. In Table 19 we identify the relevant material in CLEO II and indicate a set of reasonable possibilities for CLEO III. Significant reductions in material thickness may be obtained in both the radial and endcap directions by choosing a "thin" chamber gas and a new endplate material, by removing the intermediate tracking chambers and their associated cables, electronics, and

Table 19: Materials affecting particle identification (PID) and CsI calorimeters. The "r" represents material in the radial direction $|\cos\theta| < 0.77$; the "e" in the endcap direction $0.77 < |\cos\theta| < 0.93$.

Subsystem	CLEO II (%)	CLEO III (%)
Si Detector (r)	1.40	1.70
PT Detector (r)	0.40	–
VD Detector (r)	0.94	–
VD Mounting Hardware(e)	6.90	–
DR Inner Wall (r)	0.77	0.15
DR Gas (r)	0.43	0.18
DR Gas (e)	0.58	0.29
DR Wires (r)	0.32	0.27
DR Wires (e)	0.42	0.42
DR Outer Cathode (r)	0.95	0.95
DR Outer Wall (r)	2.0	2.0
DR Endplate (e)	35.6	20.0
DR Electronics (e)	8.9	4.9
Cooling (e)	11.0	–
DR Field Ground (e)	2.8	1.4
PT,VD,DR Cables (e)	0.5	0.5
IR Quad Support (e)	0.8	–
Total (r) affecting PID	7.21	5.25
Total (e) affecting PID	67.08	27.51
PID (e,r)	12.0	12.0
CsI support (e)	7.0	7.0
Total (r) affecting CsI	19.21	15.25
Total (e) affecting CsI	86.08	44.51

cooling, and by redesigning the DR electronics and cable plant.

The drift chamber materials listed in Table 19 can have a direct, but as yet undetermined, effect on the performance of the particle identification systems that follow. For the CsI calorimeters, the drift chamber material plus that of the particle identification system affect the performance. For CLEO II, this amounts to 19% X_0, 12% X_0 from the time-of-flight and 7% X_0 from the crystal support structure. For CLEO III, the corresponding number is approximately 17% X_0, 10% X_0 from the particle identification system and 7% X_0 from the crystal support structure.

4.3.2 Drift chamber endplate

The present DR 2 endplates are manufactured from flat 3.2 cm aluminum plates. With an elastic modulus of 10^7 psi, they deflect under the wire tension load (4.0 psi) by 0.70 cm, about 20% of the endplate thickness. A thick outer support ring is used to transfer the wire tension load to the outer skin panels and to provide a support point. The outer support ring does not provide a fixed support, as evidenced by the observed deflection in DR 2, and should be reduced in the new design.

The smaller outer radius and larger inner radius of the straight section of the CLEO III drift chamber does not necessarily allow the straight section of endplate to be half of the present thickness. Such a system would deflect by 3.6 cm if simply supported. The stresses would reach about 12 kpsi, 1/3 of the yield stress. Under these conditions it would be difficult to maintain wire position tolerances. Therefore, we are considering three alternatives for the drift chamber endplates:

1. We could use shaped aluminum endplates such as those implemented by the SLD detector. In this design the endplate radius is 1.0 m and the thickness is about 0.6 cm. The shape of the thin endplate is not stable with a simple support at the outer edges and is, therefore, maintained with a thick outer support ring. This ring would significantly degrade the photon efficiency in the region that it shadows near $|\cos\theta|$=0.80. Before we implement a similar design, it would be necessary to quantify the loss of photon efficiency in the region shadowed by the outer support ring and the gain in efficiency in the region shadowed by the thinner endplate.

2. We could retain a flat endplate design, but use magnesium which has a radiation length of 14.5 cm and an elastic modulus of 6.5×10^6 psi. Magnesium alloys can have yield points as high as 38 kpsi. A 2.9 cm thick magnesium endplate would have the equivalent radiation thickness of 0.56 of the present chamber endplate and the deflection under the wire tension load would be 0.86 cm. The maximum stress is about 5 kpsi, 13% of the yield stress. Since this deflection is with simple support at the outer radius, there is no need for an outer support ring other than what is necessary to transfer the load to the outer skin. Magnesium is very reactive but does not appear to pose a problem for the machining required to manufacture an endplate. Reaction of magnesium with chamber gases is presently being studied as part of the R&D program.

3. We could retain the flat endplate design but use a material such as carbon fiber which has a radiation length of 24.0 cm. A 5 cm thick endplate manufactured out of two 0.5 cm carbon fiber skins enclosing a 4 cm foam would have 0.14 of the present chamber endplate number of radiation lengths. This material was used as the inner support tube for the VD. It has a unidirectional elastic modulus of 45×10^6 psi[89]. With random fiber orientations, the elastic modulus is approximately half of this value. Quasi-isotropic, carbon fiber/epoxy materials are reported to have an elastic modulus of $7--15\times10^6$

psi. Using structural beams made of woven fiber with half of the fibers oriented along the length of the beam, we have observed an elastic modulus of 6×10^6 psi[90]. Our measurement using the carbon filament tube used as the inner wall of the current drift chamber is that, for a tube with half of the fibers in the longitudinal direction, the elastic modulus is $2\text{x}10^6$ psi. This wide variation indicates that the results are dependent on the details of the fabrication procedure. The strength of a composite endplate ultimately will depend on the strength of the skin material. R&D is proposed to address the suitability and use of this material.

The inner tapered section of the endplate defines and, therefore, lies entirely outside the active solid angle, $|\cos\theta| = 0.93$. Each section can then be an aluminum ring of the required thickness to provide wire positioning, mounting points for assembly, and support for the silicon vertex detector. Individual rings are joined by stainless steel hoops. With the DR 2 wire holding scheme and cell size, the stainless steel thickness is limited to less than 1.5 mm which is sufficient to hold the tension between the endplate rings.

Decisions on the above approaches are complicated by the uncertainty in the cell configuration as discussed below. The ratio of the number of field to sense wires directly affects the loads that must be supported by the endplates and the support skins.

4.3.3 Gas, wire choice, and cell design

The current CLEO drift chamber is a small cell design with 14 mm square cells, 3 field wires per sense wire, and half-cell staggering for local ambiguity resolution. The field wires are 110 μm aluminum plated with 1.6 μm of gold which contribute 0.29% X_0 of material in the current 70 cm of chamber radius. Another 0.03% X_0 of material comes from the 20 μm tungsten sense wires. We currently use argon-ethane gas with no other additives, which contributes 0.43% X_0. We are currently investigating whether to retain the rectangular cell design in the new chamber or to use hexagonal cells, also with 3 field wires per sense wire.

In order to achieve the resolution comparable to or better than the CLEO II detector in the shorter path length proposed, the scattering material in the active region of the drift chamber must be reduced to half of that in the current chamber. We therefore are considering the use of a helium based gas. With argon-ethane in a 1.5 Tesla field the present chamber shows a loss of efficiency at drift distances longer than 6 mm. Care must be made in choosing a light gas for CLEO III so as to address this problem; otherwise smaller drift cells would have to be used, adding scattering material, increasing the force on the endplates, and complicating the design. Slower drift velocity gases can also help if the problem is a question of Lorentz drift angle. Studies of different gas mixtures must be performed to demonstrate that we can achieve, and hopefully improve upon, the current spatial resolution and efficiency using a light gas in a 1.5 Tesla field.

We are considering reducing the material in the wires by using more, but thinner, field wires per sense wire. For example, in a square cell, instead of using three 110 μm field wires per sense wire, one could use seven 55 μm field wires per sense wire. These two designs have nearly the same electric field at the surface of the field wire, however, the tension to field ratio is reduced by a factor of two which may lead to electrostatic instabilities. Because the volume of the field wires in the 7 field wire design is only 58% of the volume in the 3 field wire design, it would appear that the latter design is preferable. Nevertheless, the actual improvement in momentum resolution due to multiple scattering is marginal as it comes at a significant increase in the complexity of building and maintaining the chamber. The key issues are that scattering due to field wires is only one contribution to momentum resolution, a highly non-gaussian one, and that even with 1.0 μm gold plating, as used on the recently obtained wire samples, the scattering in the field wires is due mostly to the gold. The unavoidable contributions to the multiple scattering material, those from the gas and from the sense wires, is 0.21% X_0 for a 43 layer chamber using the cell size as in the current CLEO drift chamber and a helium based gas with twice the radiation length of argon-ethane. This material creates a spread in the momentum, dp/p, which is nearly gaussian with a width of 0.271%. On the other hand, tracks that hit field wires undergo large scattering and can have their momentum measurement substantially affected.

It is necessary to consider the frequency of such hits and the fraction of the time that the momentum measurement is affected—in the 3 field wire design, only 56% of tracks hit any field wire. It is useful to compare the fraction of tracks with momentum spread less than 0.54%, roughly 2σ for the case of no field wires. In the 55 μm seven field wire design, 87.6% of the tracks and, in the 110 μm three field wire design, 86.8% of the tracks satisfy this criterion. This represents a possible gain of 0.8% in efficiency *per track* for processes where the detection is dominated by momentum resolution but at the expense of greater mechanical complexity. On the other hand, a larger increase in efficiency can by realized by reducing the thickness of the gold plating. It may be possible to reduce the gold thickness to 0.5 μm. In this case, the efficiency for the 3 field wire design increases to 88.4%, an increase of 1.6% over the same wire pattern with thicker gold plating. Similarly, the efficiency for the case of the 7 field wire design increases to 90.1%, an increase of 1.7% over the efficiency of the 3 field wire design with the same gold plating thickness.

The discussion above favors the use of a design with a large ratio of field to sense wires and a thin gold plating. Possible overriding factors are the ability to construct a chamber with greater than 3 field wires per sense wire, the reliability of aluminum wire much smaller than 110 μm, the availability of high quality, thin gold plated aluminum wire, and the ability to sufficiently define a field cage for a gas in 1.5 Tesla. Additional work is presently underway to finalize the field cage design.

Scattering material in the field wires may be reduced by using a material lighter than aluminum (X_0=8.9 cm). Carbon fiber, with a radiation length of 24 cm, would provide a factor of two reduction in the uncoated field wire material which, by extension of the example above, would result in an increase in efficiency of about 1%. The availability of durable, gold-plated carbon fibers, or other materials, with a 110 μm diameter is being considered.

Stereo wire layers are necessary to provide longitudinal measurements in the drift chamber. The number and placement of stereo wire layers not only defines the longitudinal resolution of the detector but can influence the $r - \phi$ pattern recognition and the spatial resolution as well. The CLEO II drift chamber has 11 single stereo layers separating triplets of axial layers identified in Table 20. In order to save space and provide the optimum $r - \phi$ pattern recognition, the field cage of the stereo layers is formed by the axial field wires of the adjacent axial layers. With no separate stereo field layers, the stereo sense wires effectively vary in height within the cell resulting in a longitudinal variation of the electric field configuration and, therefore, a longitudinal variation of the time-distance relationship. This variation has been difficult to calibrate, leading to a degradation of the resolution in the stereo wires from about 150 μm to about 220 μm. Alternate wire patterns are actively being studied to minimize or eliminate this problem.

The simplest way to obtain the present performance of the CLEO II drift chamber is to use the same wire pattern for CLEO III. This has the advantage that the performance is well understood. Modifications must be made, however, to account for the stepped inner section. Taking into account the obvious physical differences leads to the design shown in Table 21. In this design the last sense wire is located at 79.0 cm. We believe that such a design is well understood, and with the reduction to the material described above, will provide better performance than the CLEO II tracking system. However, the loss of efficiency at the cell edges seen in CLEO II should be corrected and means for accomplishing this are now under study.

One interesting alternate wire pattern may eliminate the variation of the height of the wire in the field cage without the addition of a large number of extra field defining layers. The configuration is shown in Table 22. There is a natural break in the chamber, between the sections of stepped and flat endplate sections, where the only transition from axial to stereo wires occurs with the addition of one extra field defining layer. This configuration may be able to minimize the cell distortion by adjusting the stereo angles of successive layers. This provides constant hyperbolic sag with dip angle resolution equal to that of the first 43 layers of the DR 2 design. This may have the consequence of an overall improvement in spatial resolution. Such a device is being prototyped to study whether this pattern does indeed enhance the resolution of stereo wires so that such a device may meet the design criteria. A tracking chamber of this type can use the unbroken group of axial layers at low momentum together with the inner silicon detector to provide the pattern recognition for tracks that curl at low radius. At high momentum, each change in sign of the stereo angle will provide an additional longitudinal measurement. One issue being studied is whether this all stereo chamber can attain equivalent pattern recognition performance to an axial/stereo chamber.

Table 20: Present CLEO II tracking wire configuration.

Wire Layer	Detector	Stereo direction
1 to 6	PTL	axial
7 to 16	VD	axial
17 to 19	DR 2	axial
20	DR 2	stereo $+1.9°$
21 to 23	DR 2	axial
24	DR 2	stereo $-2.2°$
25 to 27	DR 2	axial
28	DR 2	stereo $+2.4°$
29 to 31	DR 2	axial
32	DR 2	stereo $-2.4°$
33 to 35	DR 2	axial
36	DR 2	stereo $+2.6°$
37 to 39	DR 2	axial
40	DR 2	stereo $-2.9°$
41 to 43	DR 2	axial
44	DR 2	stereo $+2.9°$
45 to 47	DR 2	axial
48	DR 2	stereo $-3.1°$
49 to 51	DR 2	axial
52	DR 2	stereo $+3.3°$
53 to 55	DR 2	axial
56	DR 2	stereo $-3.3°$
57 to 61	DR 2	axial
62	DR 2	stereo $+3.6°$
63 to 67	DR 2	axial

Table 21: One proposed DR 3 wire configuration based on the CLEO II drift chamber.

Wire Layer	Endplate Section	Stereo direction
1 to 12	inner(stepped)	axial
13 to 15	outer	axial
16	outer	stereo $-2.4°$
17 to 19	outer	axial
20	outer	stereo $+2.6°$
21 to 23	outer	axial
24	outer	stereo $-2.9°$
25 to 27	outer	axial
28	outer	stereo $+2.9°$
29 to 31	outer	axial
32	outer	stereo $-3.1°$
33 to 35	outer	axial
36	outer	stereo $+3.3°$
37 to 39	outer	axial
40	outer	stereo $-3.3°$
41 to 43	outer	axial

Table 22: One alternate wire configuration.

Wire Layer	Endplate Section	Stereo direction
1 to 12	inner(tapered)	axial
13 to 16	outer	stereo $+1.18°$
17 to 20	outer	stereo $-1.26°$
21 to 24	outer	stereo $+1.33°$
25 to 28	outer	stereo $-1.41°$
29 to 32	outer	stereo $+1.48°$
33 to 36	outer	stereo $-1.54°$
37 to 40	outer	stereo $+1.61°$
41 to 43	outer	stereo $-1.66°$

Table 23: A survey of various aluminum wire holding schemes. For the failure rate (FR) calculation, one failure was assumed in those cases where none has been observed.

Experiment	Holding method	Number of Al wires	Wire diam. (μm)	Number of failures	Years of operation	FR/wire (10^{-5}/yr)
ALEPH ITC	Crimp/Glue	4,000	147	0	5.0	< 5.0
AMY DR	Solder	25,000	163	3	7.0	1.7
CLEO II VD	Taper Pin/Glue	2,880	142&163	0	9.0	< 3.8
CLEO II DR 2	Crimp	36,240	110	46	7.0	18.0
SLD DR	Crimp	33,000	152	0	4.0	< 0.8

4.3.4 Wire holding

Extreme care must be exercised in holding aluminum field wires. Aluminum tends to creep and any wire holding scheme must take care not to damage the wire to the point that it will break immediately or while in service. In principle, if not in practice, crimping, soldering, glueing, and combinations have been used to hold wires. However, the large number of wires in the drift chamber make this choice a critical one.

In Table 23 we provide a survey of the wire holding schemes presently in use and their reported failure rate. One observation is that the DR 2 chamber has the smallest diameter wire and the highest wire breakage rate. Our R&D program includes a serious study of wire holding schemes including the construction of prototypes.

Even though a prototype of the wire holding system can be tested and modified to reduce the number of broken wires, the final device has so many wires compared to any reasonable prototype that the broken wire count, in years of service, cannot be ensured to be zero. For example, the current CLEO drift chamber suffers from an aluminum wire breakage rate of 1 wire per 6000 wire-years. This rate can not be simulated in a prototype. Therefore, it is necessary that any wire holding method adopted for a new chamber allow for the identification and removal of broken wires.

We are presently investigating alternatives to the scheme used in CLEO II. One possible method for holding wires is a modification of that used in the current CLEO drift chamber. Wires are held and positioned by a crimp pin, insulated from the endplate by a bushing as shown in Fig. 37. Since each wire is held by a separate pin/bushing there is no problem with accessibility; broken wires can be removed by removing the associated bushing. The problem with this method comes from the crimp. To maintain a gravitational sag of 60 μm, the 110 μm aluminum wires are tensioned with 170 grams, about 60% of the yield strength. The crimp pins are copper so the wire is deformed at the crimp. Thus, the local stress is increased closer to the yield strength, increasing the broken wire rate. Fluctuations in

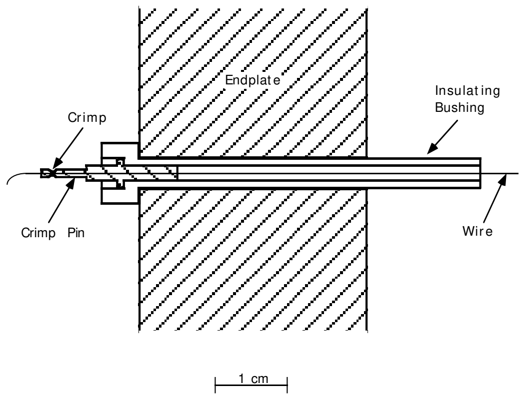

Figure 37: Wires are held and positioned by a crimp pin, insulated from the endplate by a bushing.

the dimensions of either the crimp pin, wire, or the crimping tool can also contribute to the variations in the deformation at the crimp and therefore the local stress. There are several modifications to the present wire holding method that could be employed to reduce the possibility of breaking wires. It may be that the breakage is due to variations in the dimensions of the crimp pin so that the amount of deformation of the wire is unpredictable. A quality control program where each crimp pin is measured for both inside and outside diameter could eliminate the out of tolerance pins. This may be impractical because of the difficulty in measuring an inside diameter of 170 μm. Similar pins manufactured out of aluminum would not deform the aluminum wire as much as copper pins. This would reduce the local stress on the wire but may be more susceptible to slipping. This approach has been used in SLD.

Greatly modified bushings and pins (or taper pins) could be used to allow gluing the wires after crimping thereby using both schemes independently. Breakage would then require both schemes to fail. Such a procedure has been successfully used with aluminum wires in the present CLEO intermediate tracking chamber (VD). In constructing this device we found that care must be taken not to let the epoxy run to the edge of the taper pin. If this happens any vibration may cause the wire to break on the sharp edge of the epoxy. In the case of the VD, this problem was identified and solved by putting the epoxy on the back end of the taper pin where it could not reach the wire. The wire breakage during construction was measured to be less than one part per thousand for both the taper pin and the epoxy independently. This type of problem illustrates the care that must be taken for any scheme chosen.

Our R&D program includes a vigorous plan for testing wire holding schemes. We have presently constructed a chamber similar to DR 2 and are attempting to reconstruct the failure rate we have observed over the years. All proposed designs will be tested before implementation. Tests will include some means of reliably accelerating the failure rate to demonstrate improvements over the current wire holding method.

4.3.5 Cathodes

The current CLEO drift chamber has segmented cathode readout on the innermost and outermost anode layers to provide accurate (1.2 mm) measurements in the longitudinal direction. The proposed design does not allow for a cathode readout in the inner layer because the extra scattering material between the last silicon layer and the inner drift chamber layer would degrade the momentum resolution. Furthermore, more precise longitudinal measurements will be available from the silicon vertex detector. Segmented cathode readout, similar to those in the current chamber, may be installed at the outer radius since this is outside the momentum measuring volume. Although inferior to the silicon measurements for determining the longitudinal angle, this will provide a longitudinal position measurement, more precise than can be achieved from stereo wires, for redundancy and for extrapolation into the particle identification system.

4.3.6 R&D

In the previous sections we have identified the areas of R&D necessary to complete the drift chamber project in a timely fashion. All are tightly coupled, mandating careful oversight of the individual R&D efforts. These we enumerate below:

- A gas of at least twice the radiation length of argon-ethane is required in CLEO III. Measurements of various mixtures will be performed for possible cell designs and must be capable of operating in a 1.5 Tesla field. Drift time, efficiency, and specific ionization measurements will be made in single tubular cells at zero field with the leading candidates then tested in a prototype in the CLEO II magnetic field.

- The optimum ratio of field wires to sense wires will be studied. Test chambers with a small number of square and hexagonal cells with $3:1$ ratios are being tested in the CLEO II solenoid. Monte Carlo studies need to be continued to better determine the real-world performance gain of alternative field cage designs. We also need to assess the costs of larger ratios in time and money.

- The organization and type of layers—axial or stereo—can have an impact on track finding and hardware trigger algorithms. This has to be evaluated in detail before a final design is chosen.

- The radiation length of the drift chamber endplates, support system, and electronics affects the performance of the adjacent particle identification and calorimeter systems. Alternative materials—aluminum, magnesium, composites —and alternative shapes—flat, bowed—need to be evaluated for structural strength, long term-stability, manufacturability, and physics impact.

- Mounting schemes for the drift chamber will be explored to minimize the impact of this passive structure on the particle identification and calorimeter systems, particularly in the endcap region.
- The CLEO II experience with aluminum field wires indicates that the wire holding scheme needs to be improved. This may be a refinement of the present scheme or a completely new design.
- Low mass materials (relative to Al) for field wires will be surveyed and tested if deemed appropriate.

4.4 Particle identification at high luminosities

A major goal of the physics program is to cleanly measure rare decays to test the Standard Model and be sensitive to possible new physics. This requires excellent charged hadron identification with 4σ π/K separation up to 2.8 GeV/c. All techniques for possibly attaining this quality of separation are based on Cherenkov radiation with two basic approaches utilizing thresholds or measuring the opening angle of the emitted light ring. A constraint on all implementations is that they be no thicker than 12% of a radiation length—the present time-of-flight scintillator thickness—in order not to compromise the performance of the CsI calorimeter.

4.4.1 Ring imaging Cherenkov counters

Ring imaging detectors consist of a radiator to produce Cherenkov photons, a gap to let the Cherenkov cone expand, and a photosensitive device featuring good spatial resolution. Large systems called "RICH" (or "CRID") have been constructed for the DELPHI detector at LEP and the SLD detector at SLAC. These detectors utilize gaseous radiators (C_5F_{12} or C_4F_{10}) or liquid radiators (C_6F_{14}) and detect photons using heated TMAE gas. To minimize the number of electronics channels, the photo-electrons are drifted to the end of the detector, as in a TPC, and then perform the multiplication in small proportional chambers. Since the drift time is of the order of 20 μs, these detectors are not suitable for high rate environments. Furthermore, the TMAE chambers and large electric drift fields introduce complexity and large amounts of material ($\sim$20% of a radiation length). On the other hand, there is good evidence that they work[91].

The College de France–Strasbourg group at CERN, led by J. Seguinot and T. Ypsilantis, has achieved considerable progress in the development of a simplified design called "Fast RICH" where both photon coordinates are measured at the detector surface via the pad readout of a multiwire proportional chamber with very fine pad segmentation (approximately 5×7 mm^2). Detector signals are processed by front-end digital electronics which have been developed by this group in collaboration with the Rutherford Laboratory[92]. A prototype

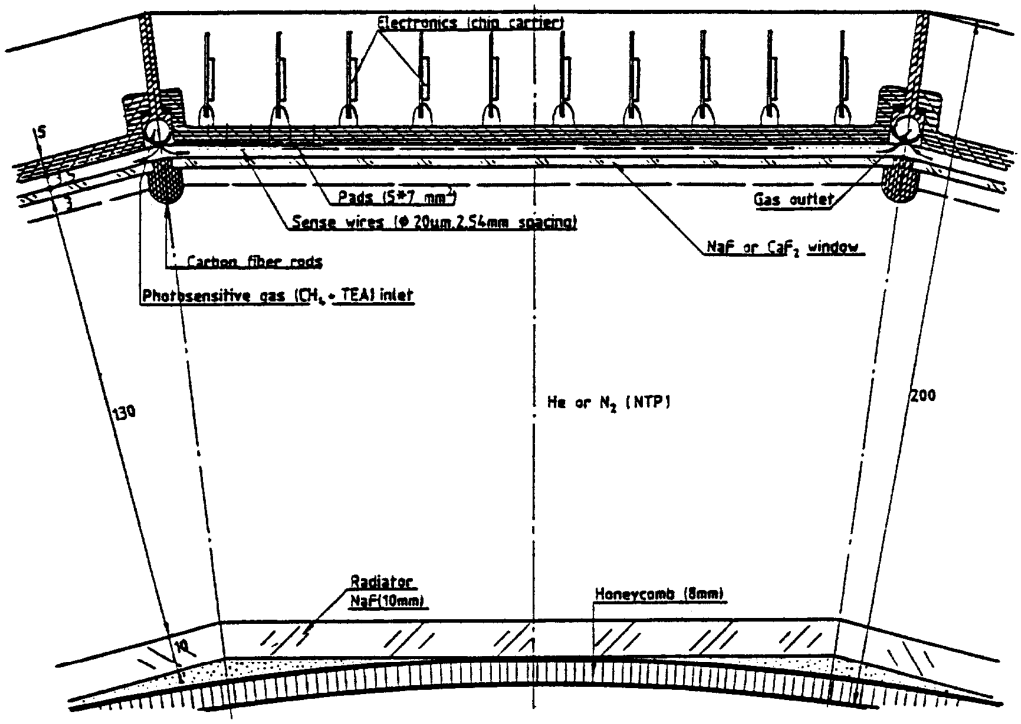

Figure 38: The detector system in use at CERN for testing RICH counters.

system has been successfully tested with cosmic rays and in hadron beams at CERN[93]. A sketch of this system is shown in Fig. 38. In this prototype the photon converter is presently TEA gas. A CsI photocathode is being fabricated and will be tested in this detector[94].

For CLEO III, we propose to use liquid radiators (C_5F_{12} or C_6F_{14}). A sketch of two possible systems, both of which are ~9% of a radiation length, is shown in Fig. 39. For the barrel region, the proximity focus system is proposed while a spherical mirror focus seems to be best for the endcap. The latter detectors could be a good match to the proposed reconfiguration of the crystals in the endcaps. In Fig. 40 the momentum for 4σ particle separation is shown as a function of incident particle angle. The curve is generated assuming a 2.5×2.5 mm^2 effective photodetector pixel size and an average quantum efficiency of 28%[95]. The minimum separation occurs at the barrel, endcap transition.

The proposed liquid radiator is being prototyped and will be tested at CERN using a CsI photocathode in early 1994. Also in 1994, a new detector with CsI photocathodes will be tested and compared with the previously used solid radiators (LiF and CaF_2). This test is crucial since one critical issue for RICH is whether the average CsI quantum efficiency between 6 eV and 7 eV can be maintained at the 15–28% level over a long period of time. Several groups have reported measurements of CsI quantum efficiency with a large spread in the results—approximately a factor of 2. It has been argued that this is due to poor handling of the photocathode material and variations in the conditions of the measurement. For example, the electric field and chamber gas appear to effect the efficiency, but the extent of these effects is controversial. Two measurements are shown in Fig. 41[94, 96]. Initial

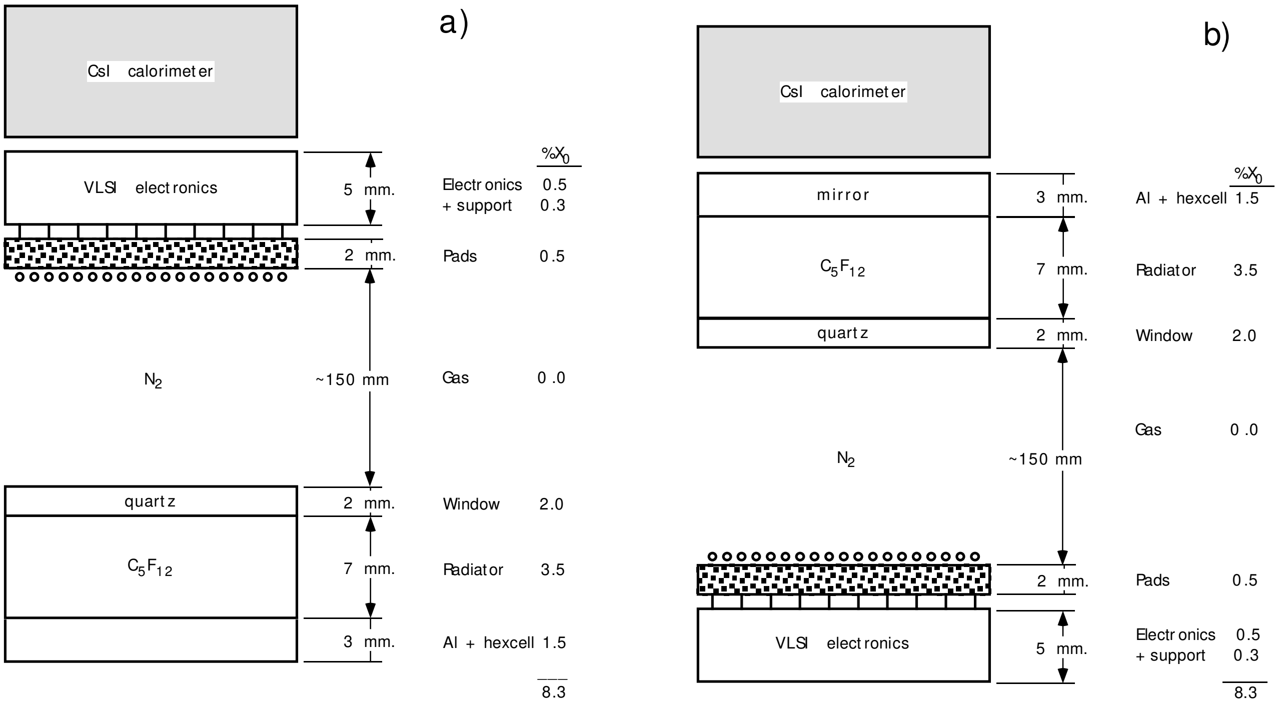

Figure 39: Possible RICH configurations with estimates of material thickness: a) proximity focus system and b) system where the mirror acts as a focussing element—in the endcap region this would be a spherical mirror.

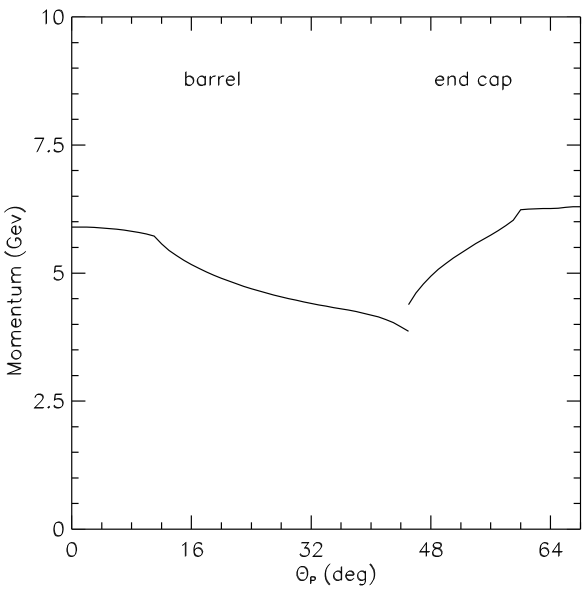

Figure 40: The momentum for 4σ π/K separation as a function of the dip angle (Θ_P) for a proximity focussing system in the barrel and a spherical focussing system in the endcap.

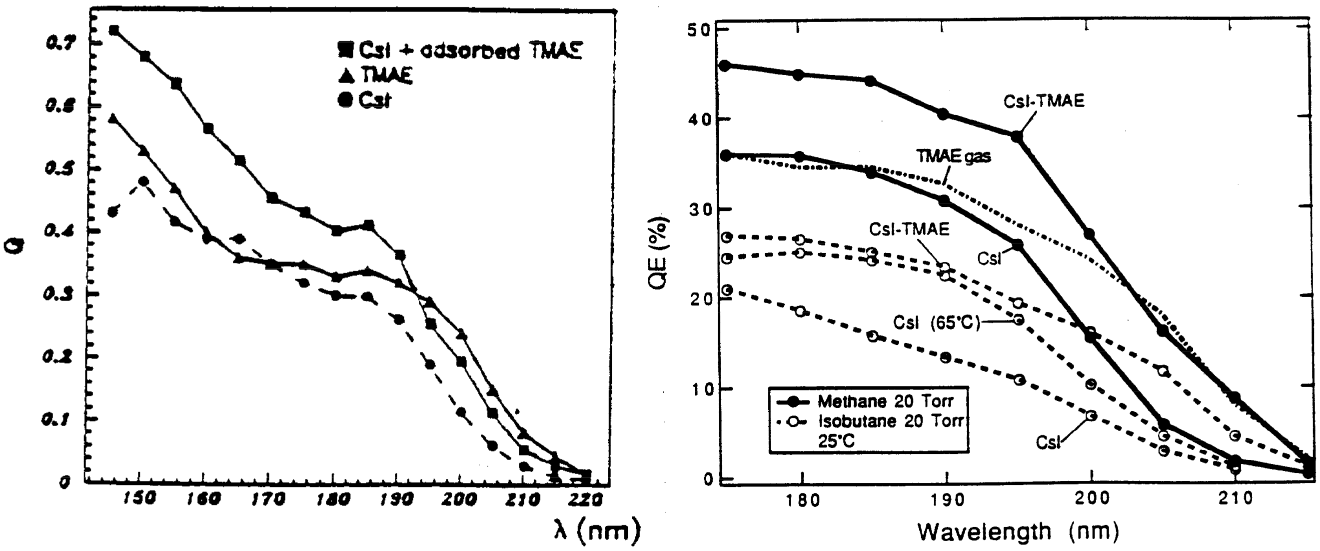

Figure 41: Measurements of CsI quantum efficiency from Seguinot *et al.*[94] on the left and Anderson *et al.*[96] on the right.

tests indicate that the operation of a liquid radiator with good optical purity over a long time not be a problem. The DELPHI experiment[97] has shown that a variety of techniques can be used to achieve this goal. In particular, the particle separation obtainable with 15% efficiency is good. As part of an R&D program, we have started work on techniques for producing and testing CsI photocathodes.

4.4.2 Aerogel

Threshold Cherenkov counters have been used successfully in particle physics experiments for over 30 years. For a particle of mass m and a radiator with an index of refraction n, the momentum threshold for light emission is given by

$$p_{thres} = \frac{m}{\sqrt{n^2 - 1}}. \tag{15}$$

If the number of protons expected in the data sample can be neglected, a single threshold Cherenkov counter with appropriate choice of the index of refraction is sufficient for π/K separation. In an environment with significant proton yield two consecutive measurements with different Cherenkov thresholds are needed. For CLEO III, π/K separation to 2.8 GeV/c requires $n = 1.01$ to 1.02, a range achievable by silica aerogels. Several experiments and R&D projects have reported successful use of aerogel for particle identification[98]. All of them, however, reported relatively small numbers of detected photons per unit length of radiator. For CLEO III a minimum of 8 detected photons are needed to provide π/K separation at the 10^{-4} level. Although the 2–3% photon collection efficiency reported by the TASSO[99] and Caltech[100] studies may be sufficient, we plan to study ways to increase this efficiency. We have started an initial effort that uses aerogel with an index of refraction n=1.02 to study light yield, wavelength shifting, and light collection efficiency.

The R&D program on the aerogel for CLEO III addresses three independent aspects of the light collection. The first is a problem of relatively small transmittance of produced light to the photodetector. Most of the Cherenkov photons are produced with short wavelengths in the UV region while the photodetectors used in previous studies were sensitive to photons in the visible range of the spectrum. A test of the light collection efficiency with UV sensitive photodetectors may lead to significant improvement. An alternate approach is to use a wavelength shifter coated photodetector to shift the wavelength of the UV photons into the visible light range and thus improve the effective light collection efficiency.

The second problem is associated with light absorption in the aerogel. The transmission spectra show very low transmittance for photon wavelengths up to about 300 nm and then a rapid rise to about 80% at 600 nm. This large self absorption for UV photons is due to Rayleigh scattering effects since the average path length between the production point of UV photons and an external photodetector is comparable to the absorption length, hence most photons are absorbed before reaching the readout device. On the other hand, the transmittance of the aerogel for the visible light photons is high. Two paths to recover the short wavelength photons are being pursued. One intersperses a thin layer of wavelength shifting compound within the silica aerogel. This can be achieved by sandwiching thin layers of UV transparent plastic (*e.g.,* 50 μm thick acrylic) coated with the wavelength shifters between 2 cm thick sheets of aerogel. In this arrangement the average path of the UV photon before it reaches the wavelength shifter is relatively short, much smaller than its absorption length. A large number of such wavelength shifting compounds with large Stokes shifts are available and there are several laser dyes that can shift UV photons into the 600 nm range. The other path uses plastic fibers doped with wavelength shifter in order to minimize the path of UV photons to the readout system. These fibers are dispersed within the radiator.

The third problem is related to the operation of photodetectors in a magnetic field. The response of photodetectors in a realistic arrangement is being studied. This includes a conceptual design of an aerogel detector that can fit into the available space of CLEO III. Among the candidates are the phototubes used in the CLEO II endcap time-of-flight counters, their variants with UVT windows and UV sensitive photocathodes, avalanche photodiodes (APD), and vacuum APD's.

4.4.3 Cherenkov correlated timing

Cherenkov correlated timing (CCT) is a new particle identification technique[101] based on using precision timing measurements to determine the Cherenkov angle of photons emitted by particles passing through a quartz radiator[102]. As opposed to conventional imaging designs, the Cherenkov light is not projected onto a large position-sensitive detector surface. Instead, the correlation between the Cherenkov angle and the path-length of totally internally reflected photons is exploited and fast timing is used to deduce this path length.

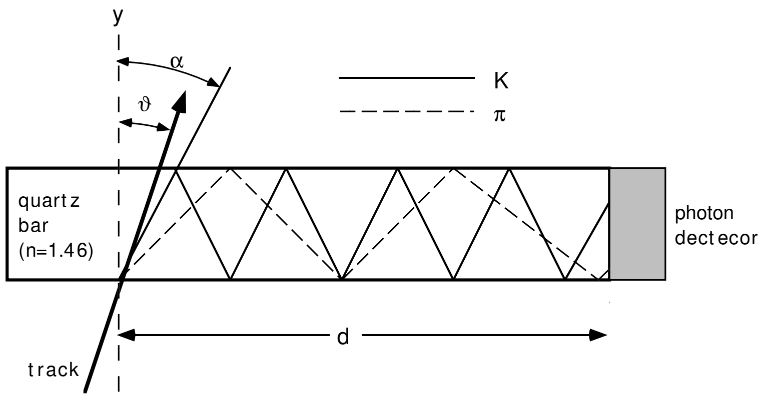

Figure 42: Principle of Cherenkov correlated timing.

This very simple principle is illustrated by the 2-dimensional example shown in Fig. 42. A charged particle traverses the quartz bar. The track angle θ and the entrance point are known with sufficient accuracy from the central tracking system. If the particle is fast enough, it will radiate photons at the Cherenkov angle χ which is related to the particle's velocity and the refractive index n of the medium by the simple equation $\cos\chi = 1/(\beta \mathrm{n})$. The photons hit the quartz/air boundary at an angle $\alpha = \theta + \chi$, and if α is greater than the critical angle $\sin^{-1}(1/n)$, the Cherenkov photon will be trapped inside the rod via total-internal reflection. The length of the photon's path as it bounces toward the end of the rod is a function only of the distance d and the angle α. For the photons shown in Fig. 42, this length is simply given by $L = d/\sin\alpha$. Since the speed of light in the rod is known, L can be deduced and the Cherenkov angle $\chi = \alpha - \theta$ can be found by measuring the flight time of the photons to reach the end of the quartz bar.

Fig. 42 also shows the exaggerated difference in flight path for light emitted by pions (dashed) and kaons (solid). Clearly, for the same values of d and θ, the light from a K will arrive later at the photon detector than the light from a π. The arrival time of the Cherenkov light at the photon detector has two components: the flight time of the particle from the interaction point to the radiator bar, and the time it takes for the Cherenkov light to propagate from the creation point to the end of the radiator. Since for a given momentum a K is slower than a π, the two components add constructively resulting in a device whose ultimate resolution is bounded from below by that of a conventional time-of-flight system, and having much better performance in most circumstances.

A CCT detector has several potential advantages:

- It is compact.
- It is fast. The latency time is determined only by the speed of light and the response time of the photon detector. Hence a CCT detector can be used in the first trigger level.
- It is simple. Measuring times accurately does not require complicated position sensitive

photon detectors and large projective geometries, but relies rather on a small number of compact phototubes.

Disadvantages are:

- Two centimeters of quartz has a radiation length of 24%, about twice that of the CLEO III design requirement.
- Due to the cylindrical geometry of CLEO III, the separation quality is a function of the angle from the beams and does not meet the 4σ requirement at all angles and momenta.
- A suitable configuration for the endcap region is not obvious.

A detailed Monte Carlo simulation[101] was developed to investigate the feasibility of a CCT detector. The prototype detector used in the simulation is shown in Fig. 43 and consists of individual $2 \times 4 \times 350$ cm^3 quartz bars surrounding a cylindrical tracking volume with dimensions consistent with the CLEO III detector. Uncertainties in the measured track angles θ and ϕ are taken to be 1 mrad and 0.5 mrad respectively. For the photon detector, a photomultiplier tube is modeled with realistic photocathode efficiency and a single electron transit time jitter of 230 ps (FWHM)[103]. The figure of merit is the number of σ's of π/K separation and is defined for this device as

$$\mathrm{n}_\sigma = \frac{(\mathrm{t_K} - \mathrm{t}_\pi)}{\sqrt{\frac{1}{2}(\sigma_\mathrm{K}^2 + \sigma_\pi^2) + \sigma_\mathrm{t}^2}} \tag{16}$$

where $\mathrm{t_K}$, t_π, σ_K, σ_π are the means and standard deviation of the K and π distributions respectively. σ_t (= 50 ps) is a constant component representing additional uncertainties in measuring the arrival time, mainly due to the longitudinal size of the beam bunches in the storage ring. A summary of our results is given in Table 24. These results indicate that our simple CCT model detector should deliver good π/K separation for particles with momentum up to 2 GeV/c. For a reduced range of polar angles, $\mathrm{n}_\sigma > 2$ is maintained up to 3 GeV/c.

An R&D effort to experimentally assess the key parameters of the CCT technique and test findings of the Monte Carlo simulation has begun. Several bars of high quality UV transparent quartz have been purchased, along with ultra-fast phototubes and appropriate readout electronics. A scintillator telescope has been constructed to provide rough measurements of the positions and angles of incident cosmic rays, as well as serving as a trigger for the stand-alone data acquisition system. The photon yield and timing characteristics of a variety of geometries and radiator/detector combinations will be investigated. Alternatives to the prototype design discussed above will be explored, including the use of UVT plastic rather than quartz to reduce the thickness of the device, and the possibility of increasing the quantum efficiency of the photon detector by replacing the phototubes by UV-enhanced APD's[104].

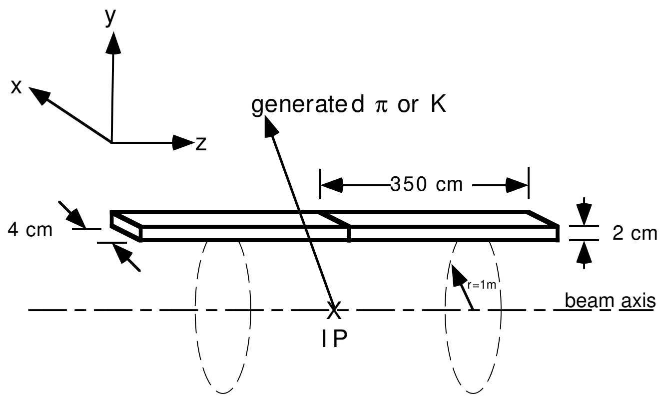

Figure 43: Geometry of a reference CCT detector.

4.4.4 High pressure Cherenkov tubes

The use of pressurized gas Cherenkov radiators is being investigated. To achieve π/K separation in the region from 0.8–2.8 GeV/c with simple threshold counters requires one radiator. A refractive index of $n = 1.0154$ gives thresholds of 0.79 and 2.8 GeV/c for pions and kaons respectively. Since the photon yield vanishes at the Cherenkov threshold, one might choose to run at a slightly higher index, somewhere between $n = 1.0154$ and $n = 1.02$, near the upper limit of easily achievable indices.

The simplest configuration uses thin-walled cylindrical pressure vessels with reflective inner surfaces to direct the light to photodetectors at the ends. Deviation from this simple shape requires additional material and complicates the mechanical design. For the barrel region the detectors would be arranged in a cylinder with the tubes parallel to the beam axis and two layers would be used to insure continuous azimuthal coverage. The 20 cm space allotted to particle identification in CLEO III allows tube diameters up to 10.4 cm and lengths of $2.5 - -3$ m. To achieve $n = 1.0154$ requires a pressure of about ~230 psi for SF_6, a high-index non-explosive gas with good UV transmission down to 150 nm; $n = 1.02$ is achievable at about 300 psi, beyond which point the room temperature liquefaction point of SF_6 is

Table 24: Number of σ's π/K separation *vs* θ and p for a CCT detector.

		θ									
		0^o	5^o	10^o	15^o	20^o	25^o	30^o	35^o	40^o	45^o
	1.0	38.3	31.6	26.1	21.6	18.1	15.7	13.5	11.6	10.7	9.6
	1.5	15.6	13.0	10.6	9.0	7.3	6.4	5.7	4.7	4.4	3.8
P	2.0	8.5	7.3	5.8	4.8	4.0	3.6	3.2	2.5	2.4	1.9
(GeV/c)	2.5	5.4	4.4	3.8	3.1	2.6	2.1	1.7	1.5	1.5	1.8
	3.0	3.9	3.2	2.4	2.2	1.6	1.7	1.2	1.2	1.1	0.9

reached. We are discussing the feasibility of measuring the UV transmission characteristics of pressurized SF_6 with various companies.

There are several potential advantages to a high pressure Cherenkov detector. These include:

- Intrinsic speed – signal production is instantaneous, transport to detectors defined by the speed of light, and signal development by the response time of the photodetector. This is particularly relevant for low-level triggering.
- Simplicity – of the order of 1000 channels of ADC readout.

Disadvantages are:

- Material thickness
- Safety concerns
- Inhomogeneous placement of material in front of the calorimeter
- Variation of the light collection with polar angle

It appears possible to build a system which contains a minimal amount of material. An infinitely long, 7.5 cm diameter cylindrical aluminum vessel with 0.8 mm wall thickness should hold a pressure of 600 psi. Tests on 1 m long, 7.5 cm diameter aluminum tubing (6061-T6 alloy/temper) of 0.8 mm wall thickness showed some failure in the glue joint of the end plugs at pressures which ranged between 450 psi and 600 psi but no damage to the body of the Al tube. With a 1 mm wall thickness and 10 cm diameter, two layers of tubes would present (at normal incidence) a maximum of 25% and an average of 5% of a radiation length of material. For beryllium the corresponding numbers are 6% maximum and $< 2\%$ average radiation lengths. Carbon fiber/epoxy laminate tubes with 2.5 mm wall thickness represent about 25% maximum and 5% average radiation lengths. It should also be possible to reduce the wall thickness by using stronger carbon fibers, at some increase in price. To these estimates, we must add the contribution of SF_6 which is about 6% of a radiation length at 300 psi.

The tubes are lined with a mirrored surface to route the light to the photodetectors. We are manufacturing aluminized mylar with a magnesium fluoride over-coating and expect the reflectivity between 200 nm and 550 nm to average close to 90%. Kapton and PEEK substrates are also being investigated. For a straight cylinder, there is a decrease in the transmission efficiency between 70 and 110 degrees. A design with a double-sided mirror halfway along the length of the tube slanted at 5 degrees to the tube axis is being modeled. Preliminary Monte Carlo studies indicate that sufficient numbers of photons can be detected if the reflectivities are high enough. In another design the tubes will be lined with a reflecting grating. Another possible variation in light collection would have the light directed to the photodetectors by total internal reflection down a coaxial wave-shifter bar (or rod). Grande and Moss[105] have shown that conversion efficiencies exceeding 90% can be achieved with a mixture of p-terphenyl and bis-MSB in an acrylic film for wavelengths between 200 and 400 nm, along with attenuation lengths of > 1 meter. A more venturesome scheme eliminates the transport of the photons altogether by proposing long photosensitive "strips" either on part of the tube surface or located coaxially within the tube. With the proper optical design, most photons would be incident on the photodetector after only one or two reflections.

For photodetectors we are investigating UV-PMT's (which must operate in a 1.5 Tesla field), APD's, and CsI thin-film photocathodes in a parallel-plate gas avalanche chamber. The latter may be applicable to the coaxial photodetector scheme mentioned above. If the photodetectors can resolve single photon pulse heights, it is possible to obtain some particle separation above the K threshold of 2.8 GeV/c. The resolution will depend on uniformity of collection and signal/noise in the photodetector.

Monte Carlo studies have been used to compare the numbers of collected photons per path length of pions and kaons for the "ideal" configuration and $n = 1.02$ above the kaon threshold. From photon statistics alone, the π/K separation for a 10 cm radiator is approximately 3.8σ, 3.4σ, and 2.6σ in the momentum intervals 2.5–3.0 GeV/c, 3.0–3.5 GeV/c, and 3.5–4.0 GeV/c.

4.4.5 R&D

In addition to the technical details already discussed for each of the techniques, a critical part of selecting the particle identification system for CLEO III will be its ability to do the physics of interest. This requires both R&D and detailed Monte Carlo simulation.

A general Monte Carlo framework is being established for the following:

- Evaluate each technology for detection efficiency and rejection ratio. This includes the performance over all angles and with realistic mechanical structures.

- Simulate the performance in the presence of backgrounds from interactions in nearby material including splash back from the CsI calorimeter.

- Simulate the impact of the particle identification material on the CsI calorimeter performance.

- Evaluate the physics impact of eliminating the endcap detectors and extending the barrel detector from 77% to 83% of 4π.

Below we identify the R&D program for each specific technology.

RICH

- Continue the CERN beam tests.
- Investigate the quantum efficiency of CsI photocathodes.
- Optimize the front-end electronics—a digital system has simpler electronics but a larger number of channels, while an analog readout of the pads with interpolation could reduce the channel count dramatically.

Aerogel

- Quantify the photon statistics that can be reliably achieved in a large system. Bulk material and sandwiches of aerogel/wavelength shifter will be studied.
- Develop photodetectors with the requisite light sensitivity and immunity to magnet fields. Candidates are mesh UV-PMT's and APD's.

CCT

- Investigate the use of materials with longer radiation lengths than quartz.
- Develop photodetectors with the required timing, noise, and magnetic immunity requirements.
- Develop a device that works in the endcap region.

High pressure tubes

- The viability and safety of a large number of high pressure, low mass containment vessels has to be demonstrated.
- Different pressure vessel materials and thicknesses need to be evaluated to minimize the material.
- While SF_6 has been discussed, there may be other suitable gases. For SF_6 and any other gases, determination of the UV transmission properties is essential.
- As discussed above, schemes to make the light collection more uniform over the whole angular acceptance of CLEO III must be developed.
- Evaluate or develop a suitable photodetector—PMT, APD, or CsI deposited cathode.
- Develop a device that works in the endcap region.

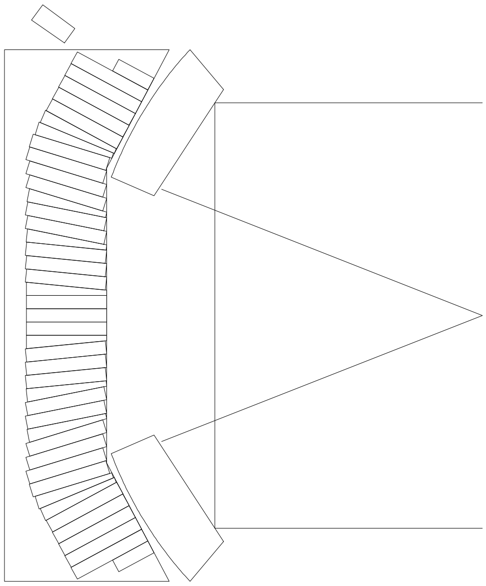

Figure 44: A side view of the endcap region of CLEO III showing a possible rearrangement of the endcap crystals to achieve a more projective geometry.

4.5 CsI endcap calorimeter

4.5.1 Mechanical modifications

The CLEO II endcap calorimeter is incompatible with the CESR upgrade because there will be a fixed vertical support column in the middle of the endcap region in order to provide a stable support for the accelerator and detector components near the IR region. On the positive side, the CLEO III detector design minimizes the gap between the endcap and the barrel calorimeters which exists in the CLEO II detector by creating room near the beam pipe for the routing of the cables from the inner detectors. This means that the solid angle coverage of the endcap and the barrel calorimeters can be made to overlap. Additionally, employment of a projective geometry in the endcap calorimeter will improve its performance, particularly at the low energies, since a reduced number of crystals will be hit by photons. This in turn will reduce the effects of electronics noise on the energy and position resolutions and also reduce the probability that two adjacent showers overlap. These considerable improvements will be obtained by redesigning the endcap calorimeter for CLEO III.

Figure 44 is a sideview of the CLEO III detector with the proposed endcap design. Figure 45 shows a quarter of the endcap viewed from the interaction point looking down the beam pipe. The squares in the figure represent the front faces of the endcap crystals. The x and y coordinates correspond to $\tan\theta\cos\phi$ and $\tan\theta\sin\phi$. The two quarter circles represent the front face of the end barrel crystals. Though the overlap between the barrel and endcap crystals is not perfect, this design shows a substantial improvement over CLEO II.

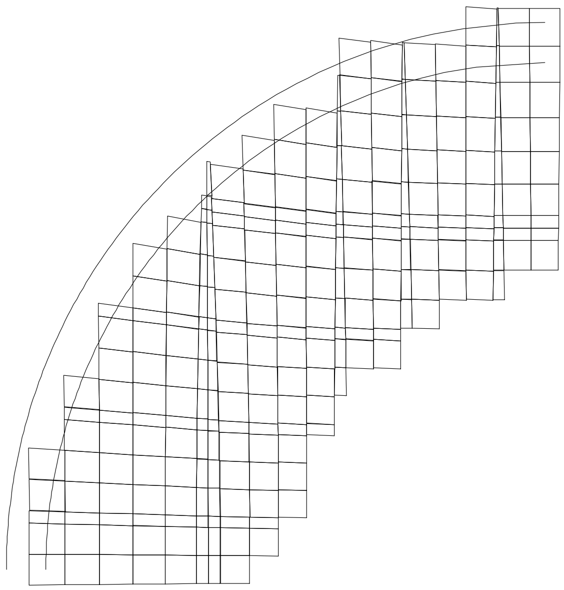

Figure 45: Interaction point view of a quarter of one the CsI endcaps.

4.5.2 R&D

Some of the issues which require R&D efforts are the following:

- We are investigating reducing the amount of material needed to support the entire endcap, particularly in front of the crystals and between the endcaps and the barrel. Accomplishing this objective while maintaining the mechanical integrity is a major design challenge. A structural analysis of each design needs to be performed.

- Remanufacturing the endcap into a projective geometry requires substantial machining of the existing rectangular crystals. Monte Carlo simulation is needed to understand the probable performance gains and their physics implications. This effort has already started.

- In order to achieve a projective geometry, there are two possibilities. Either we use a small number of highly tapered crystals, leaving others rectangular or we modestly taper most crystals. The effect of tapering on the longitudinal light-output uniformity must be understood before we can make a selection between these two options.

- To achieve a projective geometry requires the purchase of additional crystals. Arrangements with industry need to be explored.

4.6 IR mounting and assembly sequence

4.6.1 Mounting system

A primary concern in the design of the tracking system has been to eliminate, as far as possible, any structural material in the active tracking region. This is accomplished by holding the quadrupoles from sturdy pedestals in the magnet poles that are fastened to the fixed magnet yoke as shown in Figure 46. The beampipe, silicon detectors, and drift chamber are supported from this yoke without a permanent support tube crossing the active tracking volume. Nevertheless, during assembly it is necessary to have such a support tube to hold the beampipe, rare-earth cobalt (REC) quadrupoles, and silicon detectors as this subassembly is slipped into the drift chamber. Providing this space for a temporary support structure is a defining feature of the tracking system design, but the design does not preclude the use of a thin permanent support tube if the need arises.

The tracking volume is divided into two regions: the space from the beampipe to a radius of about 15.7 cm, which is occupied by the silicon detector, and the space from about 17.5 cm to 82 cm, which is occupied by the drift chamber. The annular region from 15.7 cm to 17.5 cm is reserved for the temporary support structure. This space is sufficient to provide a rigid support for the REC quadrupoles and clearance to extract the structure without damage to the detectors. To allow for extraction, the mounting structure must not only clear the outer radius of the silicon detector but also the cables and cooling tubes of the silicon detector and the REC quadrupoles.

The separation of the interaction quadrupoles into REC and superconducting parts is a crucial part of the design. The two REC quadrupoles are captured on the vacuum chamber and all three must be installed as a unit through the drift chamber. These quads are relatively small in radius and simple—they do not require the complicated electrical and cryogenic connections, nor the vacuum jacket of a superconducting magnet. This significantly reduces the clearance required through the drift chamber and allows for a larger, unobstructed, momentum measuring volume. On the other hand, the superconducting quadrupoles are not captured on the vacuum chamber and may be installed separately from each side. When installation is complete, the REC quadrupoles will be fastened to the superconducting quadrupoles, which are fastened to "keyhole" steel supports in the poles, which are in turn fastened to the fixed portion of the magnet yoke.

After installation, the silicon detector will be supported independently by the drift chamber. The beryllium beampipe, masks, shielding, and vacuum chamber extensions on each end will be supported by the quadrupoles with clearance to the silicon detector to provide the best isolation of the silicon detector from the storage ring. The option of supporting the beampipe assembly through the support of the silicon, leaving clearance to the quadrupoles, is left as an option.

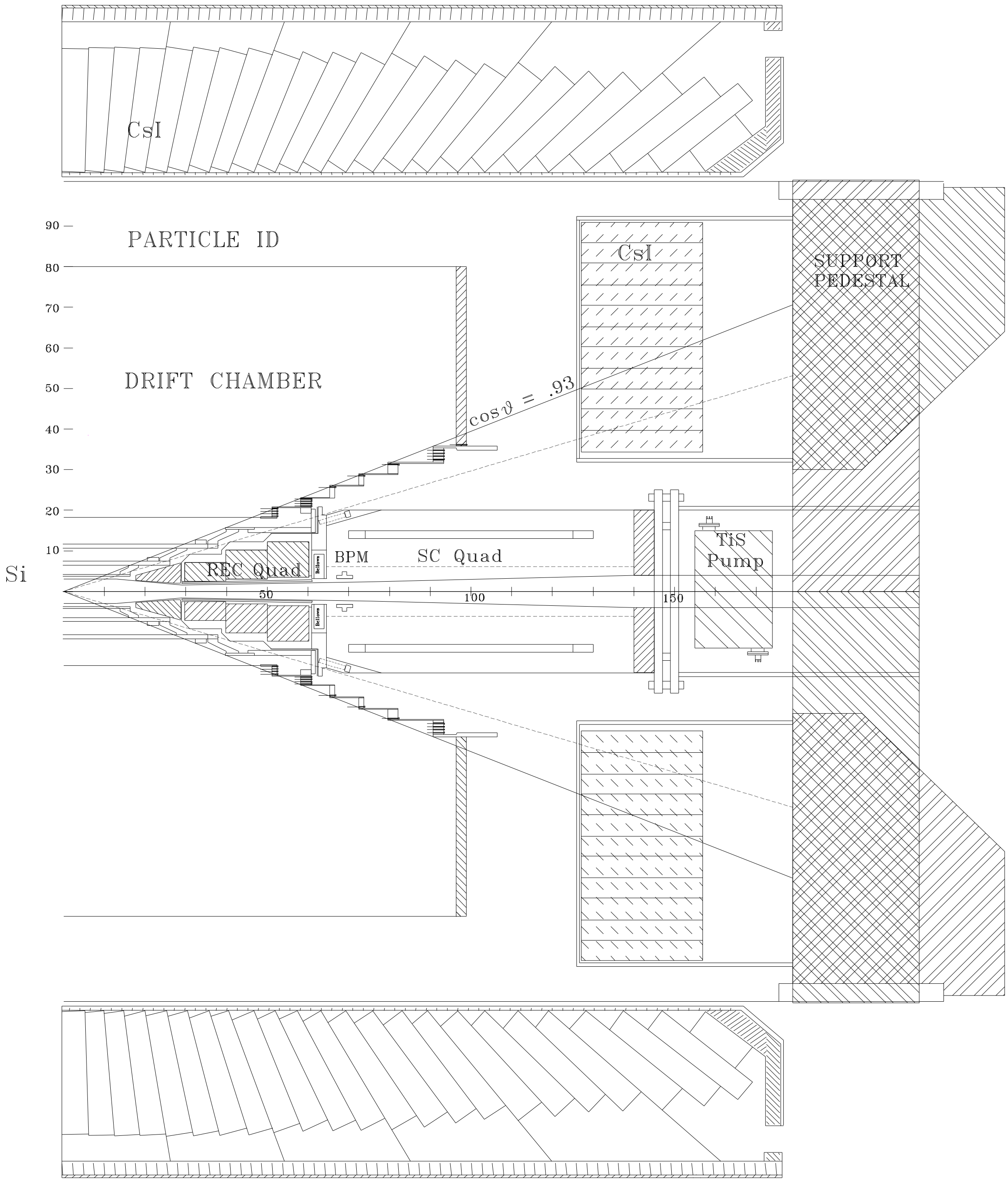

Figure 46: The CLEO III interaction region after installation of the CESR components including the beam pipe, REC and superconducting quadrupoles, and vacuum pumps.

4.6.2 Assembly sequence

The subassembly consisting of the beampipe, vacuum chamber extensions, REC quadrupoles and silicon detector will be assembled in a fixture away from the magnet yoke. Since the REC quadrupoles and shielding material weigh a few hundred kilograms and cannot be allowed to place much stress on the thin beryllium beampipe or the silicon detector, the assembly fixture must provide independent support and alignment capability for the REC quadrupoles. The REC quadrupoles will be slipped over individual vacuum chambers before the flanges on these chambers are welded in place. After appropriate vacuum procedures and testing, these flanges will be sealed to the beryllium beampipe flanges. This results in an approximately 3 m long subassembly. There will be shielding material, cooling connections and other operations to complete at this stage (Fig. 47a).

The silicon detector will next be assembled around the beampipe while the subassembly is supported in the fixture. Attachment will be made through temporary brackets to the REC quadrupoles as shown in Fig. 47b.

With the silicon detector completely mounted, wired, and plumbed, temporary longitudinal braces will be connected. These occupy the radius from 15.7 to 17.5 cm radius and attach through temporary brackets to the REC quadrupoles as shown in Fig. 47c. The longitudinal braces also attach to a stiffening ring on each end to connect the braces independently from the attachment to the quadrupoles and to provide a means of lifting the completed unit from the ends. Thus, the two quadrupoles are rigidly attached to each other, independent of the initial assembly fixture, and the entire subassembly may be picked up for installation in the drift chamber.

At this stage the new drift chamber will be installed in the magnet (Fig. 48a) and supported at its outside edge by its final "crown"-type support similar to that used for DR 2. (Alternatively, the new drift chamber may be held by temporary supports which will be replaced later by the final supports to the "keyhole" section of the magnet.) The installation of the new DR 3 will be similar to the technique used for DR 2, namely, a long beam is inserted through the axis of the whole detector on which the drift chamber rides on wheels.

The subassembly of beampipe, silicon detector, and REC quadrupoles will then be slipped through the drift chamber (Fig. 48b). The brackets holding the silicon detector to the longitudinal braces will be removed and replaced by brackets fastening to the drift chamber (Fig. 48c). Brackets that temporarily support the REC quadrupoles from the tapered section of the drift chamber end plate will replace those that attach the quadrupoles to the longitudinal braces. By completing this sequence at each of eight azimuthal positions in series, the fragile components are never stressed. The temporary longitudinal brace/stiffening ring assembly is then free and can be removed.

The superconducting quadrupoles will be introduced from each end (Fig. 49a) and fas-

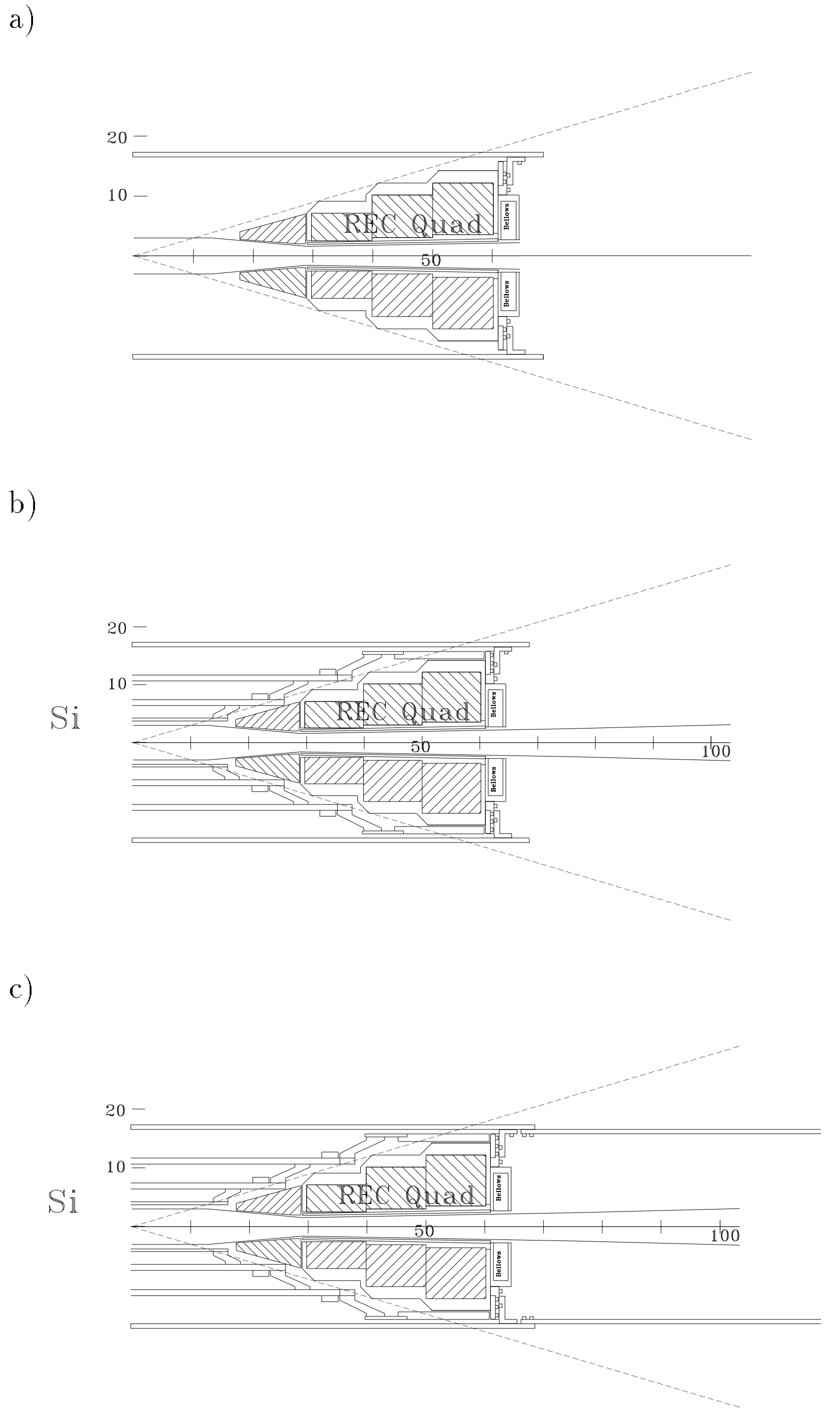

Figure 47: Assembly of the beampipe, silicon detector, and REC quads. In a), one REC quad is shown mounted around the beam pipe along with the bracing connecting it to the opposite quad. In b), the silicon dectector is mounted and temporarily attached to the REC quads. In c), the longitudinal braces are attached and the assembly can be lifted.

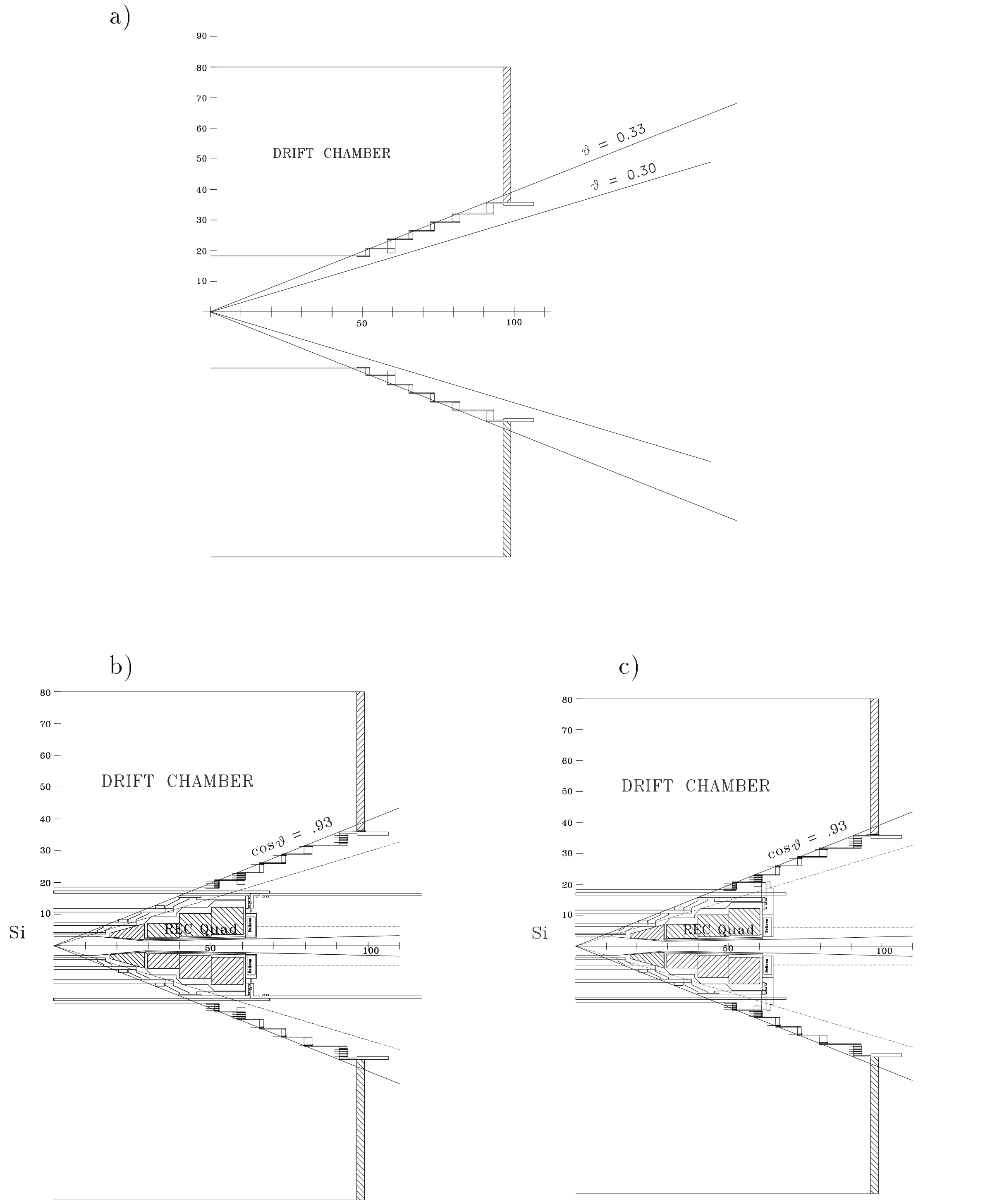

Figure 48: Insertion of the beampipe, silicon detector, and REC quad into the drift chamber. In a), the drift chamber outline is shown before insertion. In b), the beampipe, silicon detector, and REC quad have been inserted into the drift chamber bore. In c), the silicon detector and REC quad support has be transferred to the drift chamber endplates and the longitudinal bracing removed.

tened to the final "keyhole" supports (Fig. 49b). The REC magnets will be fastened to the superconducting quadrupoles and released from the drift chamber. This completes the transfer of support of the REC quadrupoles from the longitudinal braces to the fixed magnet yoke and the transfer of the support of the silicon detector to the drift chamber. The beampipe, quadrupoles, and detectors can then be surveyed and aligned. The drift chamber electronics, cabling and utilities will be installed to complete the installation.

4.7 Detector backgrounds

Beam induced detector backgrounds have been studied in the tracking system proposed in this report. The simulation and its predictive ability have been described elsewhere[106]. The CESR Phase 3 lattice with 0.5 A per beam, a crossing angle of 2 mrad, and a residual gas pressure in the ring of 3.5×10^{-9} Torr are used to generate a distribution of beam particles and photons scattered from the gas and a distribution of synchrotron photons generated by the transverse acceleration of beam particles in the magnetic structure of CESR. These distributions are input to the GEANT-based CLEO simulation where the tracking system has been altered to conform to the CLEO III design and input to a detailed simulation of x-ray scattering for the synchrotron radiation component. The GEANT geometry used is shown in Fig. 50. Occupancies in the first layer of the CLEO III DR are compared with the present performance of DR 2. Occupancies in the first layer of the CLEO III silicon detector are compared with those expected from the CLEO II/SVX upgrade.

In the CESR Phase 3 interaction region most of the masking of the detector is accomplished by the superconducting quadrupoles that are placed close to the interaction point. The only additional masking that is needed are small tungsten inserts in the regions 20.0 cm $<$ z $<$ 29.0 cm. These inserts provide a tip at $z = 26.0$ cm that shields the beryllium beam pipe from direct synchrotron radiation hits. The inside of the beryllium pipe is coated with 10 μm of gold that provides a further factor of 2 reduction in the flux of x-rays that strike the first layer of silicon.

Table 25 shows the breakdown of detector backgrounds for the CLEO III upgrade. The backgrounds are low and they compare favorably with the CLEO II/SVX upgrade. For CESR Phase 2 with a total beam current of 600 mA, the occupancy in the first silicon layer is expected to be 0.04% and the present DR 2 has an occupancy of 0.27% for each microsecond of detector exposure time. While the predicted occupancies are ten times better than what is required for good track reconstruction efficiency—1%/μsec in the silicon and 10%/μsec in the drift chamber—another iteration of mask optimization could improve the backgrounds even further.

Under the masking scheme proposed, the silicon detector and on-board electronics will be exposed to 30 krad/year. The electronics must be able to tolerate a minimum of 150 krad total exposure which will require their fabrication in a rad-hard process.

a)

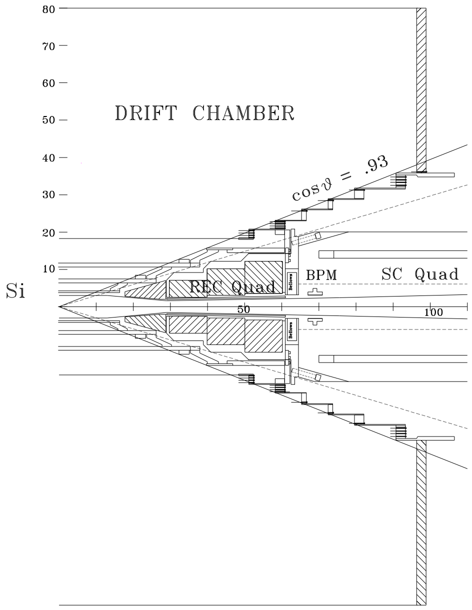

b)

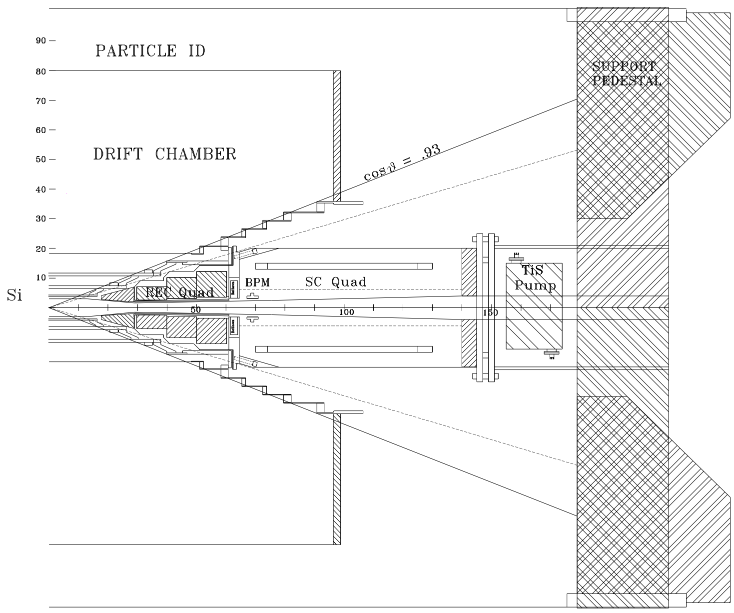

Figure 49: Installation of the superconducting quads. In a), the superconducting quad is inserted, bolted to the REC quads, attached to the support pedestal, and the REC quad support disconnected from the drift chamber. In b), the installation is complete. The silicon detector is supported from the drift chamber and the quads, beampipe, beam position monitors, and vacuum pumps are supported from the keyhole pedestal in the CLEO magnet pole piece.

Table 25: Predicted occupancies in the CLEO III tracking system. Occupancies are in % per microsecond of detector live time.

Source	Silicon Layer 1	DR Layer 1
Beam Gas	0.055	0.82
Synchrotron	0.017	0.00
Total	0.072	0.82

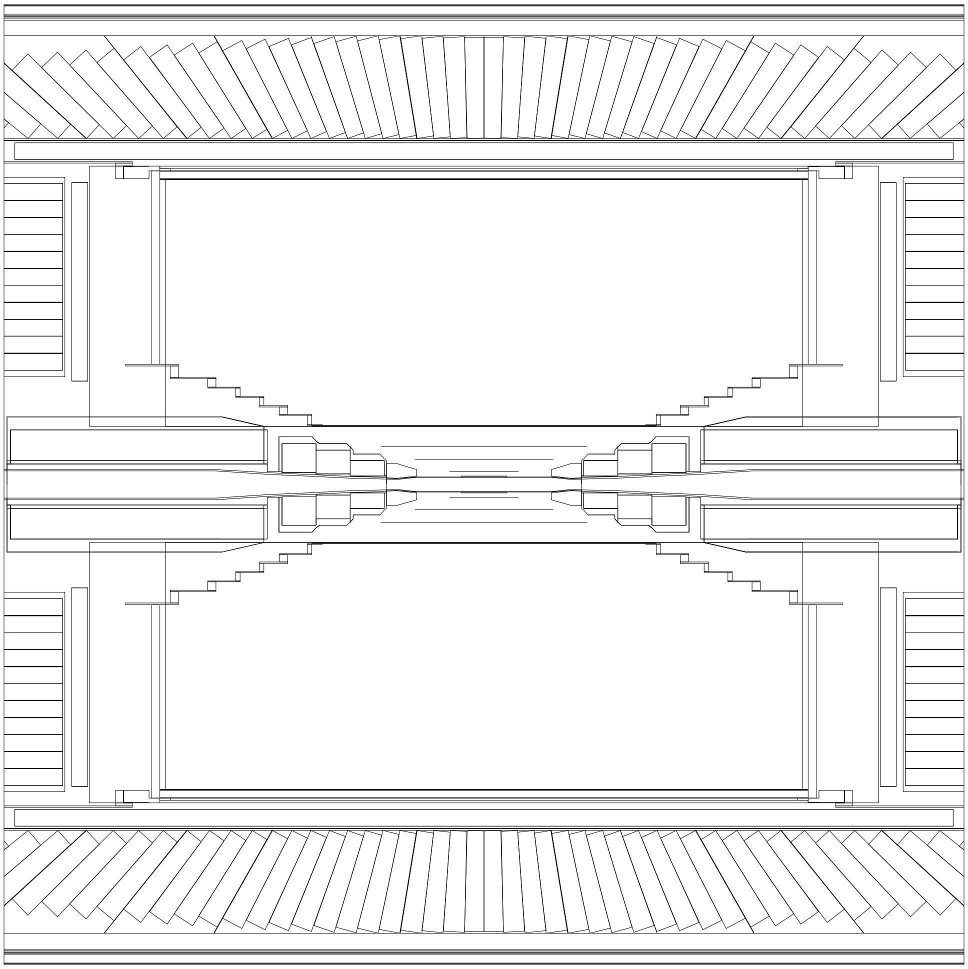

Figure 50: Model of CLEO III and CESR Phase 3 used in particle and synchrotron radiation background studies.